Revealing the role of oxygen on the defect evolution of electron-irradiated tungsten: A combined experimental and simulation study

Zhiwei Hu, Qigui Yang, François Jomard, Pierre Desgardin, Cécile Genevois, Jérôme Joseph, Pär Olsson, Thomas Jourdan, Marie-France Barthe

Revealing the role of oxygen on the defect evolution of electron-irradiated tungsten: A combined experimental and simulation study

Zhiwei Hu [a], *Qigui Yang* [b, e, f], *François Jomard* [c], *Pierre Desgardin* [a], *Cécile Genevois* [a], *Jérôme Joseph* [a], *Pär Olsson* [b], *Thomas Jourdan* [d, *], *Marie-France Barthe* [a, *]

[a] CEMHTI, CNRS, UPR3079, University of Orléans, F-45071 Orléans, France

[b] KTH Royal Institute of Technology, Nuclear Engineering, Roslagstullsbacken 21, 114 21 Stockholm, Sweden

[c] Groupe d'Etude de la Matière Condensée, CNRS, UVSQ, 45 avenue des Etats-Unis, 78035 Versailles cedex, France

[d] Université Paris-Saclay, CEA, Service de recherche en Corrosion et Comportement des Matériaux, SRMP, F-91191 Gif-sur-Yvette, France

[e] Institute of High Energy Physics, CAS, 100049 Beijing, China

[f] China Spallation Neutron Source, Institute of High Energy Physics, CAS, Dongguan 523803, China

Keywords

Tungsten, Electron irradiation, First-principles calculations, Cluster dynamics, Frenkel pairs recombination, O-vacancy complexes, Positron annihilation spectroscopy

Abstract

The evolution of Frenkel pairs has been studied experimentally and theoretically in tungsten, a Body-Centered Cubic metal. We used positron annihilation spectroscopy to characterize vacancy defects induced by electron irradiation in two sets of polycrystalline tungsten samples at room temperature. Doppler Broadening spectrometry showed that some positrons were trapped at pure single vacancies with a lower concentration than expected. At the same time, positron annihilation lifetime spectroscopy revealed that positrons are annihilated in unexpected states with a lifetime 1.44-1.64 times shorter than that of single vacancy (200 ps), namely unidentified (X) defects. Secondary ions mass spectrometry detected a significant concentration of oxygen in these samples, of the same order of magnitude as electron-induced single vacancy. In addition, Cluster dynamics simulated defect behaviors under experimental conditions, and Two-component density functional theory was used to calculate defect annihilation characteristics that are difficult to obtain in experiments. Finally,

by combining the theoretical data, we simulated the positron signals and compared them with the experimental data. This enabled us to elucidate the interactions between oxygen and Frenkel Pairs. The X defects were identified as oxygen-vacancy complexes formed during irradiation, as oxygen is mobile in tungsten at room temperature, and can be trapped in a vacancy, while its binding to self-ion atoms leads to their immobilization thus reducing defect recombination. Therefore, we anticipate oxygen to play an important role in the evolution of tungsten microstructure under irradiation.

1. Introduction

Refractory metals are essential in future nuclear industrial infrastructure, thanks to their high melting point, high thermal conductivity, and low sputtering rate. For instance, tungsten and its alloys [1–5] are the most mentioned candidates as plasma-facing components and divertor in fusion applications [3,4,6]. In future fusion power plants, they will be exposed to high fluxes of Hydrogen (H) and Helium atoms and will have to withstand intense neutron irradiation. Such extreme conditions modify the crystal structure, displacing atoms from their initial lattice sites, and creating Frenkel pairs (FPs) i.e. a displaced self-interstitial atom (SIA), leaving a vacant site (single vacancy, V_1). The diffusion and interaction of FPs induce other defects (voids, dislocation loops, vacancy complexes, etc.), at the origin of microstructure evolution [7], which is harmful to materials [8–11], degrades their properties [8,12], and then limits reactor performance [13–15]. Hence, understanding microstructural evolution is a preliminary step towards improving, adapting materials, and extending the active service life of future fusion power plants.

Electron irradiation is an efficient method to induce isolated FPs in metallic materials and can be used to study defect properties in detail. Was and Allen claimed that the FP production rate is near 100 % in nickel (Ni) with 1 MeV electron [16]. Numerous resistivity recovery (RR) experiments on electron-irradiated metals were realized in the 70s-80s [17–19], revealing the

different defect evolution stages, in which Stage I was attributed to the migration of SIAs. In iron, Body-Centered Cubic (BCC) metal, Takaki et *al.* [20] isolated two sub-stages of Stage I, i.e. I_{D2}, and I_E, corresponding to the recombination of correlated and uncorrelated FPs. Twenty years later, Fu et *al.*[21] have obtained similar results by performing simulations based on kinetic Monte Carlo. For Face-Centered Cubic (FCC) metals, RR experiments in electron-irradiated platinum showed a recombination fraction of 63 % for non-correlated FPs [22]. In tungsten, due to the high mobility of SIAs, a non-negligible population of electron-induced FPs should be recombined. However, the recombination rate (*Rc*) in this material is still an unsolved issue.

Furthermore, light-element impurities (LEs) may play an important role on the defect evolution. Lu et *al*. [23,24] summarized numerous theoretical works and showed that vacancy-oxygen (O) and carbon (C) complexes can bind with hydrogen (H) atoms and act as H-trapping sites. These complexes can be germs for clustering of H which is considered as the origin of the blisters observed in tungsten [25,26].

Experimentally, we also demonstrated that LEs act on the evolution of vacancy-type defects in self-ion irradiated tungsten [27]. While the effect of C [28,29] has been addressed in numerous works, the effect of O on the behavior of defects in tungsten has yet to be studied, particularly with experimental methods. In vanadium, Zhang et al.[30] argued that the hardening induced by dislocation accumulation is not sufficient to explain their experimental data suggesting that the missing strain hardening component is due to oxygen-vacancy complexes and conclude that detection of such defects is very challenging.

Positron annihilation spectroscopy (PAS) was demonstrated to be a well-adapted technique to characterize vacancy-type defects [31,32]. The complementarity of Doppler Broadening and lifetime spectroscopies makes it possible to quantify the vacancy defects and access their nature using simulation [33–35]. Accordingly, in the present work, we have combined theoretical and

experimental studies to better understand the properties of defects and the impact of O on the PAS signals and defect recombination. We investigated the behavior of FPs in a typical BCC metal, i.e. tungsten, using 2.5 MeV electron irradiation at room temperature (RT) to introduce a quantifiable fraction of FPs. We employed PAS and, as a complement, transmission electron microscopy (TEM) to characterize damaged samples. In addition, secondary ion mass spectrometry (SIMS) was used to quantify the LEs in our samples. In terms of theory, we chose Cluster dynamics (CD) which has proven to be an appropriate and accurate method for simulating the evolution of simple homogeneously dispersed defects in metals [36] such as those induced by electron irradiation. Furthermore, referring to the promising findings that have been discovered for vacancies in tungsten[37], we have used Two Component Density Functional Theory (TCDFT), to calculate the positron annihilation characteristics -lifetime and Doppler broadening spectrum- for various vacancy-oxygen complexes. Finally, we applied the positron trapping model [31,38] to calculate positron annihilation signals in irradiated samples using CD and TCDFT data. The comparison of calculations with experimental results highlighted the effect of O on the evolution of defects during irradiation.

2. Methods

2.1 Material and irradiation conditions

High purity (HP, 99.95 wt.%) tungsten samples ($7 \times 7 \times 0.3$ mm^3 plates, and Ø3 mm discs) were purchased from Neyco (**Nc**) and Goodfellow (**GF**) companies. The Nc samples were mechanically polished and annealed at 1600 °C for 1 hour under high vacuum (~ 10^{-7} mbar) to eliminate the native and polishing-induced defects. However, this temperature was insufficient to eliminate all the defects for the sample recently purchased from Goodfellow (GF series). The annealing temperature was subsequently raised to 1700 °C, and the duration was extended to 3 h. After the annealing, a few discs were electropolished to create thin areas in the center, using Tenupol-5 with a double jet of NaOH solution (0.05 mol. L^{-1}, 20 °C, and a voltage of 15 V) for

10 min. The configuration of the samples i.e. plates and thinned discs was adapted to the characterization techniques i.e. PAS and TEM, respectively.

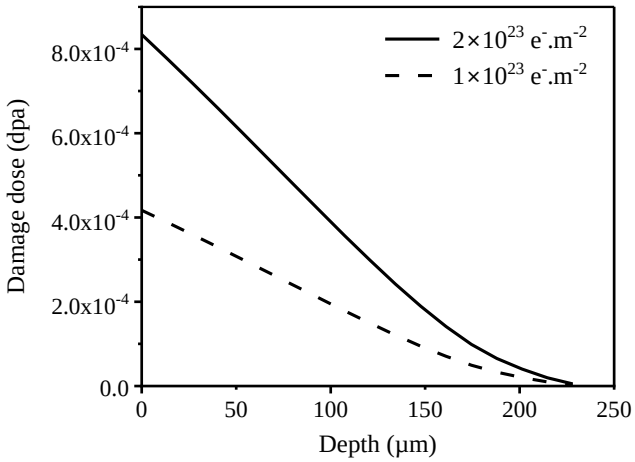

Fig.1: Calculated damage profile of 2.5 MeV electrons in tungsten using POLY ET SMOTT program for two fluences LF: 1 × 10^{23} m^{-2} and HF: 2 × 10^{23} m^{-2}

2.5 MeV electron irradiations were performed using the SIRIUS accelerator [39] at Laboratoire des Solides Irradiés (LSI). The tungsten samples (plate: **Nc**, disc: **GF**) were damaged with an electron flux of ~5.5 × 10^{17} m^{-2}. s^{-1} at about 50 °C for 2.5 and 5 days, to obtain two fluences, namely a low fluence (LF: 1 × 10^{23} m^{-2}) and a fluence twice as high, the high fluence (HF: 2 × 10^{23} m^{-2}), respectively. The damage dose was calculated using the POLY et SMOTT program [38–40] with a threshold displacement energy of 55.3 eV [43]. The estimated damage profiles, i.e. displacement per atom (dpa) as a function of depth are plotted in Fig.1. For both fluences, the damage dose decreases linearly until 150 µm and becomes negligible beyond 220 µm. Within the maximum slow positron penetrated region (~700 nm in tungsten [44]), the damage dose can be considered approximately constant, corresponding to an average value of about 8.33 × 10^{-4} dpa for HF, and 4.16 × 10^{-4} dpa for LF with the same standard deviation of about 1 × 10^{-6} dpa.

2.2 Experimental characterizations

2.2.1 Positron annihilation spectroscopies

When a positron penetrates the solid, under interaction with the host atoms, it is thermalized and diffuses into the lattice. During the diffusion phase, the positron encounters an electron, and the electron-positron (e^-–e^+) pair is then annihilated by emitting gamma rays. In a perfect lattice, a positron annihilates in a delocalized state called "lattice state". If a positron finds open volumes along its diffusion path, it has a high probability of being trapped [31,32] in such vacancy-type defects, where it experiences relatively weak coulomb repulsion from the nucleus. Once the positron is trapped, it annihilates in this localized state, the vacancy defect-related state. The electronic density is different in each annihilation state (lattice or different types of vacancy defects). Therefore, the annihilation characteristics vary from one defect to another. This makes PAS a sensitive and widely used technique for probing vacancy-type defects in materials [31,32]. For this reason, Slow Positron Beam Doppler Broadening Spectroscopy (SPB-DBS) and Positron Annihilation Lifetime Spectroscopy (PALS) measurements were employed to characterize the electron-induced defects in tungsten.

A Doppler Broadening spectrometer is coupled to a slow positron accelerator at the CEMHTI laboratory [45]. This instrument provides a variable monoenergetic positron beam, with energies ranging from 0.5 to 25 keV. The positron beam has a diameter of 1 mm and moves over a 3 mm spot as its energy increases from 0.5 to 25 keV. The penetration depth of slow positrons can be estimated by the Makhovian model [46]. For the highest energy (25 keV), the positron reaches a maximum of ~700 nm in tungsten [44]. In the SPB-DBS measurement, Doppler Broadening - or emitted gamma rays - spectra, corresponding to the momentum distribution of annihilated e^-–e^+ pairs, are recorded using a high-purity germanium detector as a function of positron energy *E*. The dead time of the spectrometer is about 10 % and the energy resolution of ~1.25 keV (full width at half maximum, FWHM), equivalent to a momentum resolution of 4.89×10^{-3} m_0c (m_0: electron mass, c: light speed). Gamma-ray detection efficiency is higher than 25 % at 1.33 MeV. From each DB spectrum, the low momentum ***S***

and high momentum ***W*** annihilation fractions or parameters can be extracted. They are the ratio of the count number in defined momentum ranges over the total count in the spectrum. The momentum ranges are between 0 - |2.64| × 10^{-3} m_0c for ***S***, and (|9.80| - |24.88|) × 10^{-3} m_0c for ***W***, respectively. To further investigate the defect distribution in the sample, the VEPFIT program [47,48] is used to model the sample as several homogenous layers and convert ***S*** and ***W*** measured as a function of positron energy i.e. ***S(E)*** and ***W(E)*** into a depth profile i.e. ***S(z)*** and ***W(z)***. Each layer has specific annihilation characteristics i.e. ***S***, ***W***, and an effective diffusion length L_{eff}^{+}, which is physically linked to the defect concentration, and the intrinsic diffusion coefficient of positrons.

Compared to DB measurement, PALS is more quantitative, in particular for determining the nature of the defects. For this study, a fast positron-emitting source was fabricated by deposing ^{22}NaCl on 6 µm-thick aluminum foil. The encapsulated source is a square of about 4×4 mm^2. and the ^{22}Na enriched NaCl salt deposit has a maximum diameter of 3 mm at the center. The source was sandwiched between two equivalent samples (7 × 7 mm^2). By detecting the gamma photons emitted simultaneously to the birth (1.274 MeV), and the annihilation (~511 keV) of the positron, using two fast detectors in coincidence. The spectrometer resolution is a Gaussian function with a Full Width at Half Maximum (FWHM) of about 212 ps. The lifetime spectrum is a convolution of the spectrometer resolution with a sum of decreasing exponential functions, reflecting the different annihilation states experienced by positrons. The contribution of positrons annihilated in the ^{22}Na source is taken into account in the data processing. Each experimental spectrum contains more than 5 × 10^6 counts, which ensures a correct decomposition of the spectra. It is important to note that a fraction of the positrons annihilate in the source. ANAPC program was employed to deconvolve the lifetime spectra. As is generally done, three main contributions from the source are subtracted from the experimental lifetime spectrum [49,50]. These contributions depend on the quality of the source and the

nature of the samples. In this study, the source contributions were determined from the experimental spectra of a pair of extra-high purity W samples (Plansee 99.9999 wt.%) annealed at 1700 °C for 3h. The first source contribution (C_1) has been identified as coming from the source wrapping foil and has a lifetime of 230 ps and an intensity of 23.59%. Its intensity is calculated using the Bertolaccini formula given in [51]. The second component (C_2) corresponds to the annihilations in the NaCl salt itself and or at the surface of the wrapping foil. The corresponding lifetime is 450 ps. The third one (C_3), generally weak, is due to annihilations of positronium probably formed on the surface of the samples or in the air between them [49,50]. The corresponding lifetime is 1500 ps. The intensities of the two longest correction sources are estimated at (1.3 ± 0.3) % and (0.35 ± 0.05) %, respectively. Apart from these source contributions, a single compound of the Lattice was revealed of about 103 ps.

The measured annihilation parameters (lifetime and $\boldsymbol{S}$, $\boldsymbol{W}$) depend on the specific annihilation characteristics of the lattice, $\boldsymbol{X_L}$, and traps *i* detected by the positron $\boldsymbol{X_i}$ (where $\boldsymbol{X}$ is given for $\boldsymbol{S}$, $\boldsymbol{W}$ or lifetime), and on the trapping rate $\boldsymbol{k_i}$ being the product of their respective concentrations $\boldsymbol{C_i}$ by their specific trapping coefficient $\boldsymbol{\mu_i}$. The relationship between measured annihilation parameters (lifetime and $\boldsymbol{S}$, $\boldsymbol{W}$) and $\boldsymbol{k_i}$ can be formulated using trapping models [38].

2.2.2 SIMS

In our previous works, we demonstrated that the LEs probably interplay with vacancy-type defects, leading to variation on the SPB-DBS signals [15,80]. DFT predicted very low migration energy for O (0.17 eV) and high interactions with vacancy-type defects in tungsten [24,52–54]. Hence, we employed SIMS to quantify O in some samples using a CAMECA IMS 7f available at Groupe d'Etude de la Matière Condensée (GEMaC). The cations and anions were collected in ultra-high vacuum (~10^{-9} mbar) by Cs^+ (15 kV, 40 nA, 23° respect to surface normal) and O_2^+ ions (5 kV, 100 nA, 45° respect to surface normal), respectively. The beams scanned

199 the sample surface over a square area of about 150 × 150 μm^2, and secondary ion collection
200 was carried out in a smaller circular area (Ø 33 μm) to avoid edge effects. The mass resolution
201 $M/\Delta M$ was 400. The ^{16}O signal is measured together with W ones as a function of time. To
202 evaluate the oxygen concentration, we applied the relative sensitivity factors (RSF) method [55]
203 determined in oxygen-implanted W samples. A profilometer (DEKTAK 8) was used to measure
204 the depth of the craters, allowing us to determine the sputtering rate, and to convert time profile
205 into depth. In addition, the error bar on the oxygen concentration determination is estimated to
206 be about 28 %.

207 #### 2.2.3 TEM

208 The irradiated thin foil was observed using a JEOL ARM200F cold field emission gun
209 electron microscope operating at 200 kV and equipped with double spherical aberration
210 correctors. The observations were carried out in the zone axis [001] at different magnifications
211 from 50 to 600 kx, in various regions of the thin part of the sample. The dislocation structure
212 was characterized by weak-beam imaging mode using various diffraction beams, i.e. g (200),
213 (020), and (110), which were used to distinguish the two types of dislocation loops expected in
214 tungsten, those with ½a<111> and <100> Burgers vectors (b) due to the extinction rule g·b=0
215 [56].

216 ## 2.3 Simulation methods
217 ### 2.3.1 Density Functional Theory

218 In parallel to the experiments, density functional theory (DFT) calculations were performed
219 with the Vienna *Ab initio* Simulation Package (VASP) [57] with the projector augmented wave
220 (PAW) [58] method. We utilized the generalized gradient approximation (GGA) with the
221 Perdew-Burke-Ernzerhof exchange-correlation functional [59] for the electron exchange and
222 correlation potential. The 4 × 4 × 4 supercells with 4 × 4 × 4 Γ-centered *k*-point mesh was used
223 to investigate tungsten. The plane-wave cutoff energy was set to 520 eV for all calculations.

The structures of oxygen-vacancy complexes, O_pV_1 (p = 1-6) were built by referring You et *al*. [53]. The $5p^6 5d^4 6s^2$ and $2s^2 2p^4$ electrons were treated as valence states for tungsten and O, respectively. The criterion of convergence for the electronic loop was 10^{-5} eV. For ionic relaxation, the force tolerance was 0.01 eV/Å.

After calculating the electron densities with the standard DFT, the positron densities were calculated using TCDFT in the relaxed structures. The TCDFT implementation used in this work was developed by Makkonen et *al*. [60] based on VASP and the details can be found in [60,61]. The Borońki-Nieminen local density approximation (LDA) [62] was used for electron-positron correlation and enhancement factor. The positron was approximated to not affect the average electron density, and the zero-positron-density limit was used [62]. This is the so-called conventional scheme. It has been shown that this scheme provides results that agree well with more self-consistent modeling due to certain compensation and feedback effects [63]. The vacancy-type defects were fully relaxed by taking into account the repulsive forces on ions induced by positron [60]. The momentum distribution of annihilated electron-positron pairs was calculated with the state-dependent scheme [64] and PAW method [58,60]. The computed Doppler spectra were convoluted with a Gaussian function with a FWHM corresponding to the experimental resolution (4.89×10^{-3} m_0c) and theoretical ***S*** and ***W*** values were extracted using the same momentum windows as in experiments.

2.3.2 Cluster dynamics

To simulate the kinetic evolution of small vacancy-O and SIA-O clusters, we used a mean field cluster dynamics approach as implemented in the CRESCENDO code [65]. Equations of cluster concentrations are solved as a function of time. Physical phenomena taken into account are: the production of defects (SIAs and vacancies) by electron irradiation, absorption of migrating clusters by other clusters and by grain boundaries, and thermal dissociation of clusters. Migration is assumed to be exclusively thermally activated, except for vacancies for which

electron-induced diffusion is also considered [66,67]. The effect of grain boundaries is taken into account through sink strengths, which also take into account the transition from 1D to 3D mobility [66]. Parameters of the model are shown in Tab. 1.

The parametrization of pure vacancy and SIA clusters closely follows the OKMC parametrization proposed by Becquart et *al.* [68]. In particular, we consider 3D mobility for vacancies and vacancy clusters, 1D mobility for SIA clusters, and mixed 1D-3D mobility for SIAs. Reaction rates for this latter case can be found in references [69,70].

We then assume that O is the only impurity acting on the clustering process, due to its rather high mobility and its strong binding with vacancies [54]. The exact concentration of O dissolved in the matrix is not precisely known experimentally. O may form oxides and migrate to grain boundaries, leading to a much lower concentration in the matrix than the one measured by SIMS. Taking into account the formation of oxides and the interaction of O with grain boundaries is beyond the scope of the present study. Instead, we perform a parametric study of the role of O, by varying its concentration as dissolved in the matrix from 0 to 220 appm. Accordingly, grain boundaries are considered only when the O concentration is zero.

In our model, Vacancy-O clusters are 3D objects that can contain up to 6 O atoms. This assumption is probably more valid for small vacancy clusters. We will see in the next section that Vacancy-O clusters indeed remain small in the present experimental conditions. These clusters are also assumed to be immobile. The binding energies of vacancies and O atoms to these clusters are deduced from formation energies calculated by DFT for O_pV_1 clusters [54]. For other cluster sizes, we determine the vacancy binding energy as the maximum of the value given by a capillary law (assuming that vacancies will essentially bind together) and the binding of a vacancy with an O atom (assuming that a vacancy will preferentially bind with an O atom). No formation of pure O clusters is permitted, as their diffusion behavior is unknown.

SIA-O clusters may also form in our model, under the form of dislocation loops trapped on O impurities. Such clusters are thus assumed to be immobile, unlike pure SIA clusters which migrate very quickly along their glide cylinder. Binding energies of O are given by an analytical model fitted to DFT results [29], whereas no effect of O on the binding energies of SIAs and vacancies to loops is considered. It is assumed that an interstitial loop cannot host more than one O atom every 2b along the dislocation line, where b is the norm of the Burgers vector of the loop.

Tab. 1: Parameters for the cluster dynamics simulations.

Parameter	**Value**	**Reference**
Temperature	323 K	EXP
Electron energy	2.5 MeV	EXP
Electron flux/damage rate	5.5×10^{17} m^{-2} s^{-1} / 2.3×10^{-9} dpa s^{-1}	EXP
Grain size	10 μm	EXP
Lattice parameter a_0	0.316 nm	-
Norm of the Burgers vector of interstitial loops	0.274 nm	-
Diffusion prefactor of v_n (n = 1, …, 3)	$4 \times 10^{-6} / (10^3)^{n-1}$ $m^2 s^{-1}$	[68,71]
Migration energy of v_n (n = 1, …, 3)	1.66 eV	[54]
Diffusion prefactor of O	3.75×10^{-8} $m^2 s^{-1}$	[72]
Migration energy of O	0.17 eV	[54]
Diffusion prefactor of I_n (n = 1, …, 10)	$1.5 \times 10^{-3} / n^{1/2}$ $m^2 s^{-1}$	[68]
Migration energy of I_n (n = 1, …, 10)	0.013 eV	[68]
Rotation frequency of a crowdion (i_1)	6.59×10^{12} Hz	[72]
Rotation energy of a crowdion	0.38 eV	[72]
Formation energy of vacancies and vacancy clusters V_n	DFT values for $n \leq 8$ Capillary model for larger sizes	[65,68]
Binding energies of O_pV_n clusters ($1 \leq p \leq 6$)	DFT values for O_pV_1 ($p \leq 6$) See text for other cluster sizes	[53]
Formation energy of SIAs and SIA clusters I_n	DFT values for $n \leq 12$, discrete-continuum model for larger sizes	[73]
Binding energies of O_pI_n clusters	DFT values and analytical model for the binding of O No influence of O for the binding of SIAs and vacancies	[69]
Recombination distance of SIAs and vacancies	$2\ a_0 = 0.632$ nm	
Absorption efficiency of SIAs by loops Z_i	1.1	

3. Results

3.1 SPB-DBS

Fig.2a shows the ***S*** parameter as a function of the positron energy *E* of pristine and electron-irradiated samples. **For the pristine sample (Nc#6)**, within the energy range from 0.5 to 25 keV, ***S*** decreases progressively with increasing positron energy ***E***. ***S*-*W*** plot in Fig.2b shows that annihilation characteristics of the bulk tend toward the ones of the tungsten ***Lattice*** (S_L = 0.367, W_L = 0.0844) which have been identified for **GF** samples in [74]. By operating the VEPFIT program, the ***S(E)*** and ***W*(*E*)** curves of the pristine sample were fitted by a single-layer model. The ***S*** (0.366 (3)), and ***W*** (0.0855(3)) of the fitted layer are close to the tungsten ***Lattice*** values, and an effective diffusion length of about 121 (4) nm indicates a low defect concentration, which can be roughly estimated below the detection limit of the SPB-DBS measurement (~10^{23} m^{-3} [74]).

For electron-irradiated samples with two fluences (LF: **Nc#1** & **3** (1×10^{23} m^{-2}) and HF: **Nc# 4,** & **5** (2×10^{23} m^{-2})**),** ***S(E)*** curves were plotted with downward and upward triangle, respectively, in Fig.2 a. ***S*** increases with the fluence at all energies higher than 2 keV. Above 2 keV, the annihilation fraction at the surface decreases quickly, due to more annihilation at the defects, ***S*** differs from the pristine sample value, and this deviation increases with positron energy. Comparable evolution is observed for the samples irradiated together at the same fluence (LF: **Nc#1** & **5** and HF: **Nc#3** & **4**). It confirms a homogenous fluence on the surface of the samples. However, the ***S(E)*** value dispersion reveals a heterogeneous distribution of defects in the **Nc** samples. ***S*** decreases until 25 keV for samples irradiated at low fluence (LF: **Nc#1** & **5**), while it only decreases up to 18 keV and then plateaus for samples irradiated at high fluence (HF: **Nc#3** & **4**). Because of this heterogeneous distribution, the homogeneous multi-layer model used in the VEPFIT program is inappropriate to fit the defect distribution in irradiated samples. Moreover, Fig.2 a shows the ***S(E)*** curve measured in **B05**, a **GF** disc

irradiated at HF at the same time with **Nc#3** & **4** plates. The ***S*** values are less dispersed in **B05** compared to other samples. When the positron energy increases from 0 to 5 keV, the ***S*** parameter decreases. Within the energy range from 5 to 25 keV, the S values fluctuate in B05 with a mean value of 0.3981 (16), in contrast to the declining trend in other samples. The ***S*** plateau value is higher than those measured in the same energy range for the irradiated **Nc** samples. Furthermore, Fig.2 b shows the ***S*-*W*** plot, for both fluences. ***S*-*W*** points are located close to the line L_1, which was identified as the characteristic line of annihilation at V_1 with the saturated point (S_{V1}, W_{V1}) [75]. These results suggest that the positrons annihilated mainly at V_1 with a more or less heterogeneous distribution in **Nc** samples. Their concentration is greater in samples after longer irradiation. The highest concentration was found in the GF B05 sample but still did not reach the saturation signal of the single vacancy (V_1 point in Fig.2) in tungsten [75].

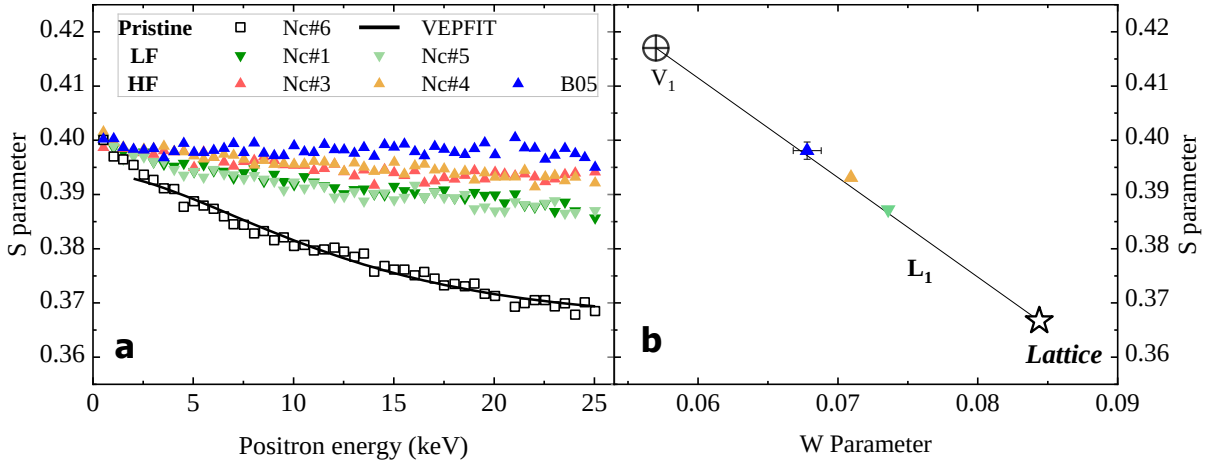

Fig.2: Annihilation characteristics of pristine sample (Neyco, square) in comparison with 2.5 MeV electron-irradiated ones at two fluences, LF 1 × 10^{23} (downward triangle) and HF 2 × 10^{23} m^{-2} (upward triangle) at RT, **a:** low momentum parameter S as a function of the positron energy E, and **b:** S versus W, fitted value (using VEPFIT) for pristine (**Nc**#6), mean values in the 5-25keV range for B05, and value at 25 keV for damaged Nc samples, with the standard deviation as the error bars.

3.2 PALS

According to the damage profile in Fig.1, 2.5 MeV electrons induce damage until about 220 µm. To complement the SPB-DBS measurements in the surface region (~700 nm), PALS was used to obtain more information on the induced defects in the in-depth bulk (the first 50

μm). Fig.2a shows processed PALS spectra (after source corrections, and deduction of background noise) of the pristine and irradiated samples: the LF pair (**Nc#1** & **5)** and the HF pair (**Nc#3** & **4)**. Obviously, after irradiation, the spectra contain longer-lifetime components.

Tab. 2: Lifetime components deconvoluted from experimental spectra using the ANAPC program for pristine and electron-irradiated sample pairs at 2.5 MeV, taking into account 3 components, the third being fixed at 200 ps.

		Component 1		Component 2		Component 3		
Fluence ($\times$ **10^{19}** *cm^{-2})*	τ_{av} **(ps)**	τ_1 **(ps)**	I_1 **(%)**	τ_2 **(ps)**	I_2 **(%)**	τ_3 **(ps)**	I_3 **(%)**	**τ_M (ps)**
0	105	105 ± 0.3	100	-	-	-	-	-
1	135	11 ± 0.1	11 ± 3	122 ± 2	56 ± 2	200	33 ± 1	62
2	147	12 ± 0.2	7 ± 2	135 ± 2	63 ± 1	200	30 ± 1	84

Using ANAPC to fit the spectra, a 105 ps lifetime component was extracted for the pristine samples. This value lies within the lifetime range of the tungsten ***Lattice***, from 100-110 ps [76–79]. For irradiated samples, we have first tested a 2-component fit. The results showed a long lifetime of 187 ± 2 and 197 ± 4 ps for High and Low electron fluence respectively and an intensity of 53 and 40% respectively. These lifetimes are close to those expected for a single vacancy. Meanwhile, a short lifetime with a value (102 ps and 127 ps respectively) close to that of the perfect Lattice in tungsten was also found for both fluences. It's noteworthy that when positrons annihilate in more than one state, for example in a deep trap (defect with no detrapping) and the lattice (delocalized state), the short lifetime indicating the time that positrons spend in the lattice before being trapped or annihilated, this lifetime should be shorter than the lifetime of the perfect Lattice. Furthermore, the τM estimated with eq.1 was 135 and 148 ps respectively, i.e. larger than that of the Lattice. This indicates at least a second trap (X defect) exists apart from the single vacancy. Hence, a 3-component fit was attempted, but the number of free parameters and the close values of the lifetime components prevented the fit. It should be noted that in these analyses, vacancy clusters larger than the single vacancy were not considered, as they are not expected to form in electron irradiation at RT: (1) due to the low energy of PKA, the local density of displacements is low and no cascade is expected; and (2) because single

vacancies are not mobile at RT, their migration energy is high i.e. $E_{V_1}^m$ = 1.66 eV [80]. To fit the data with three components, the lifetime component τ_3 was fixed to 200 ps a value previously identified for the single vacancy, i.e. 193-199 ps reported by theoretical works [82–84], and 195-200 ps obtained experimentally [75,84]. The fitted results are reported in

Tab. 2. The intensity of the third component τ_3 (fixed at 200 ps) was of approximately 30 % was for both fluences. Meanwhile, a component with a very short lifetime τ_1 of about 10 ps with a quite low intensity of about 10%, was also extracted. This component corresponds to the 'reduced lattice' lifetime, i.e. the time that positrons spend in the lattice before being trapped or annihilated. Its value is very short compared to the lifetime of the perfect Lattice because most positrons are trapped before annihilation. This indicates a minor fraction of positrons annihilated in the ***Lattice***. Such a short lifetime probably means that the limit of the deconvolution was reached. This short component was taken into account because the decomposition with three components shows the best variance compared to the two-component decomposition. In addition, a component with an intermediate lifetime τ_2 of about 122, and 135 ps was deconvoluted from the spectra of samples damaged with both fluences, i.e. LF and HF, respectively. Its intensity is about 56 % for LF and increases to 63 % for the HF. As a result, the average lifetime has increased from 135 to 144 ps (Fig.3 b), when the electron fluence has doubled, from 1×10^{23} to 2×10^{23} m^{-2}. This result suggests that, in addition to the ***Lattice*** and V_1, one or more new positron traps (X defect) were created in electron irradiation at RT. Furthermore, according to the trapping model [31], if 100 % of the positrons annihilated in the identified states ***i*** in the experiments, the sum $1/\tau_M$ of the ratio between the intensity I_i and the lifetime τ_i of each component should be equal to the reciprocal of the ***Lattice*** lifetime, i.e.$\tau_{Lattice}$. (eq.1)

$$\frac{1}{\tau_M} = \sum_1^i \frac{I_i}{\tau_i} \qquad \textit{eq. 1}$$

However, the τ_M value obtained for both fluences is shorter than the tungsten ***Lattice*** lifetime (

Tab. 2), suggesting that the positrons annihilate at more than three states.

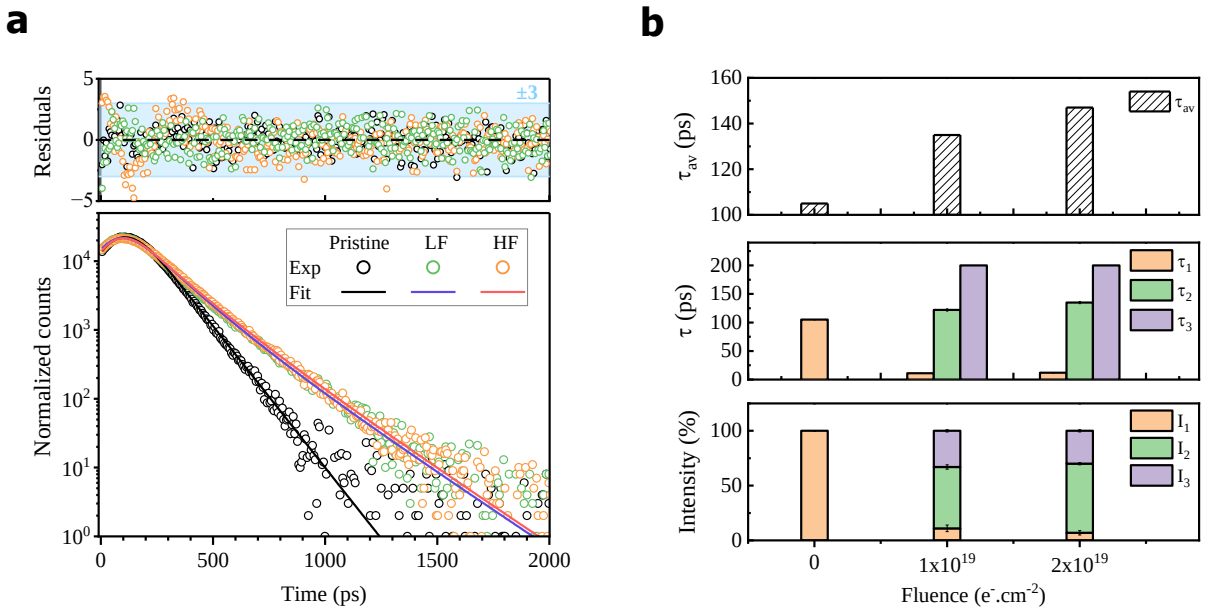

Fig.3: a) Processed experimental lifetime spectra without source correction nor background noise of the pristine and 2.5 MeV electron irradiated samples **Nc*#1*** & ***5*** *for low fluence and* ***Nc#3*** & ***4*** *for high fluence*, and b) the deconvoluted lifetime components (lifetime and corresponding intensity) and average lifetime extracted from the lifetime spectra using the ANAPC program versus irradiation fluence. The quality of the fit was checked by calculating the residual standard deviation between the experimental and fitted spectra which is ±3 over the entire time scale.

3.3 SIMS

Fig.4 a and b show the secondary anions and cations collected in **Nc#3** within a mass range from 0 to 250 a.m.u with Cs^+ and O_2^+ as the primary ions, respectively. Not surprisingly, the tungsten isotopes appear with the highest intensity. Moreover, O appears as a major impurity in spectra acquired with Cs^+ sputtering. In addition, it should be noticed that significant intensities are detected at around 200, 216, and 232 a.m.u. respectively, which probably correspond to O tungsten molecules (WO_x) for several tungsten isotopes. It should be noted that O cations collected with primary O_2^+ ions cannot be used as an argument for the presence of O in the samples, as is possible for anions collected after sputtering with Cs^+.

Then, the analysis was focused on the quantification of O, in the pristine (**Nc#6**) and irradiated samples (**Nc#3**, **B05**). Fig.4 c shows the O profiles collected by SIMS at three random positions with primary Cs^+ ions. The O profiles are both comparable for **Nc#3** and **Nc#6**, suggesting that there was no significant introduction of O during irradiation. O concentration is high at the surface and decreases rapidly, probably merely due to a native oxidized layer [85]. Beyond 200 nm, the profiles fluctuate down to 1.5 µm depth, and the concentration varies from 30 to 250 appm, depending on the craters for a sputtered area of 150 × 150 μm^2. After reducing the sputtered area to 100 × 100 μm^2, no obvious change in the O profile is observed in **Nc#6** (at ~1250 nm), while there is a decrease for one crater in **Nc#3** (at ~900 nm). We emphasized that the O concentration returns to the value of a larger sputtered area between 900 and 2000 nm. These results indicate that oxygen concentration is nonhomogeneous in the **Nc** samples. It changes not only with depth but also with the characterized area

In contrast, O profiles obtained from the HF-damaged **B05** sample are rather 'clean': concentrations from three craters are comparable. A plateau is obtained from 200 to 1500 nm. A clear decrease in O concentration was revealed after reducing the sputtering area, leading to a new plateau with a lower concentration of about 25 appm. These results suggest that the SIMS detection limit (<25 appm) of O was reached in **B05**, and its distribution is homogeneous.

To summarize, a heterogeneous distribution of O concentration was revealed in **Nc#3** and **Nc#6** (30 to 250 appm). The highest values are probably due to the presence of a significant fraction of oxide nanoparticles. The lowest values revealed that O atoms could be dissolved in the matrix with a concentration between 30 to 80 appm, as already observed in [86], in contrast, the oxygen concentration is homogeneous and less than or equal to 25 appm in the B05.

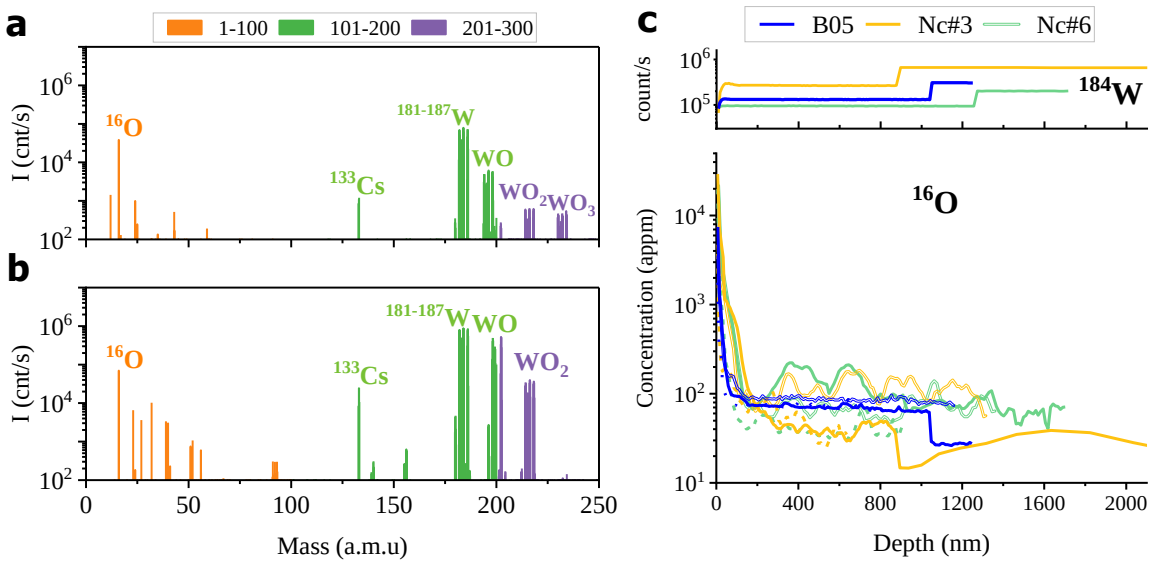

Fig.4: Mass spectra ranging from 0 to 250 a.m.u. of the secondary particles sputtered from the sample Nc#3 (2×10^{23} m^{-2}), a) collected anions with Cs^+ primary ions, and b) collected cations by using O_2^+ primary ions. c) O profiles of pristine (Nc#6, yellow), and electron-damaged –HF- (Nc#3, green), and B05 (blue) for three random positions (Crater 1 to 3) plotted using different line types.

3.4 TEM

During irradiation experiments, one tungsten-thinned disc (GF, 99.95 wt.%) was also damaged at the HF (i.e. 2×10^{23} m^{-2}) simultaneously with thick samples. No dislocation loops nor any black dots were observed (Fig.5) in the images indicating that no defects with a size greater or equal to 1 nm were created during irradiation. This size is the minimum size for which the diffuse contrast can be distinguished in TEM [87]. The thickness of the observed region was estimated using EFTEM (Energy Filtered Transmission Electron Microscopy) measurements and measures about 30 nm. Several zones over the thin region were observed for a total surface of 3×10^{-27} m^2. It follows that if some defects larger than 1 nm exist, their maximum concentration should be about 1×10^{19} m^{-3}.

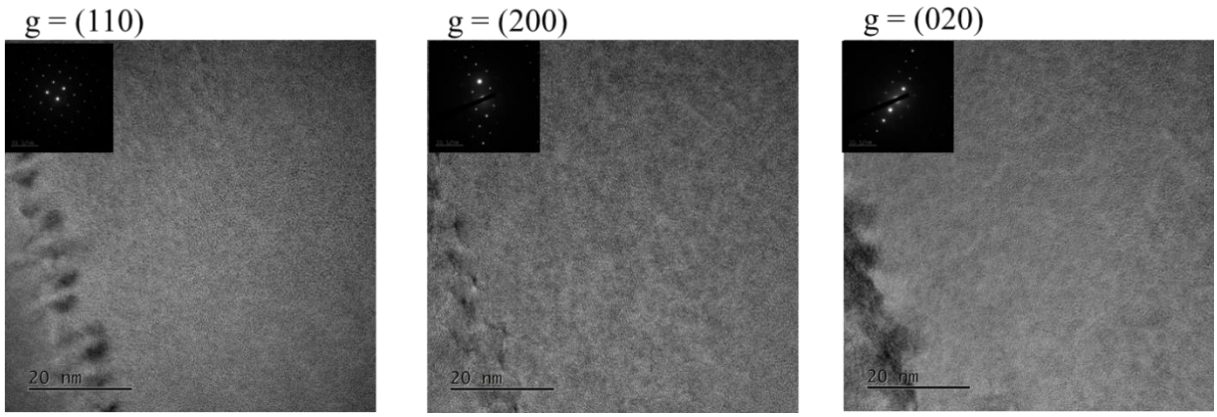

Fig. 5: bright field TEM images acquired using different g-vectors (g=(110), g=(200) and g=(020)) in a tungsten foil irradiated with 2.5 MeV electrons at RT with a fluence of 2.10^{19} cm^{-2}.

3.5 TCDFT

Since SIMS analysis shows an O concentration of the same order of magnitude as that of induced V_1, we focused our TCDFT calculations on the interaction between O atoms and V_1. Tab. 3 contains the total binding energy of oxygen-vacancy complexes and positron lifetimes calculated for O_pV_1 complexes. Our binding energy values are in good agreement with the values in [53]. The calculated positron lifetimes for annihilation in the tungsten ***Lattice*** and as trapped in V_1 are 101 ps and 195 ps respectively as already reported in [37]. These values calculated based on TCDFT are comparable with the experimental ones found in the present work.

Tab. 3: Binding energy $E_{binding}^{O_P-V_1}$, and position lifetime **τ** calculated using TCDFT-LDA for O_pV_1 *(p=1-6)* complexes, and estimated specific trapping coefficient $\mu_{O_pV_1}$ of the complexes. These trapping coefficients were estimated using the value of V_1 in Ta *[31]* for V_1 and reduced by the ratio of the Voronoi volume of O_pV_1 complexes to that of pure V_1 (0.0159 nm^{-3}) for the complexes. [a]Reference *[53]*, [b]Reference *[88]*. The error on the values of $\mu_{O_pV_1}$ is calculated from that of $\mu_{V1} = (6 \pm 3) \times 10^{-15}$ $m^{-3}.s^{-1}$ *[31]*

Number of associated O atoms, p	$E_{binding}^{O_pV_1}$ **(eV)**	**τ (ps)**	$\mu_{O_pV_1}$ **(10^{-9} $cm^3.s^{-1}$)**
1	3.0, (3.04[a])	170 (170.6[b])	4.89 ± 3.46
2	5.9, (5.96 [a])	142 (136.8[b])	3.91 ± 2.77
3	6.9, (7.29 [a])	143 (129.4[b])	3.67 ± 2.60
4	8.56, (8.80 [a])	130 (123.6[b])	2.75 ± 1.94
5	10.06, (10.37 [a])	124 (121.6[b])	2.42 ± 1.71
6	11.92, (11.21 [a])	132 (128.3[b])	2.50 ± 1.76

Tab. 3 shows that the positron lifetime of O_pV_1 complexes decreases with the number p of associated O atoms when p remains inferior or equal to 5. The lifetime of O_1V_1 is 170 ps, then drops drastically to near 140 ps for O_2V_1 and O_3V_1, and decreases to 130 ps and 124 ps for O_4V_1 and O_5V_1, respectively. Interestingly, the positron lifetime rebounds to 132 ps for O_6V_1, a result also reported in [88] with different positions of O atoms in the vacancy. These changes are due to the change in electronic density in V_1. Moreover, the positron remains localized in the center of the complex for all *p* values (see local positron density in Fig.6) indicating that trapping can be expected in all the O_pV_1 complexes. Fig.6 shows the computed ***S-W*** plot for O_pV_1 complexes. The ***S-W*** annihilation fractions are very sensitive to the presence of O atoms in the vacancy. A clear trend emerges: The ***S-W*** points move down to the bottom-right with the increasing number of O atoms. The calculated ***S-W*** points of $O_{2\text{-}6}V_1$ deviate from the line segment connecting the **Lattice** and $\mathbf{V_1}$, called L_1 in our experiments, as p increases, while that of the O_1V_1 complex is close to the middle of L_1.

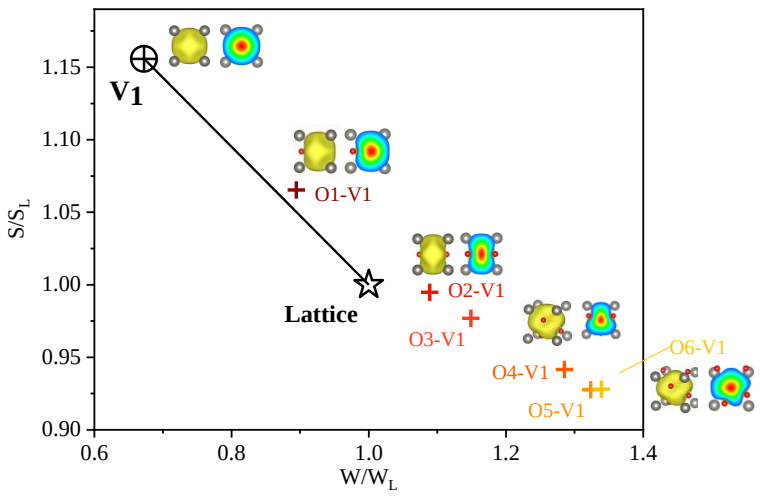

Fig.6: a-1) Theoretical **S-W** plot for V_1 associated with O atoms in tungsten. The computational results are convoluted with a Gaussian function with a FWHM of 4.89×10^{-3} m_0c, which corresponds to the experimental resolution. (-left) 3D structure –O atoms (red sphere) location in the vicinity of V_1 (gold sphere)- and (right) local positron density are illustrated for V_1, O_1V_1, O_2V_1, O_4V_1, and O_6V_1.

3.6 Cluster dynamics

Cluster distributions at HF (2×10^{23} e^- m^{-2}), for three different O concentrations in the matrix, are shown in Fig.7 (a-c). We also represent cluster distributions for $x_O = 200$ appm, when electron-induced diffusion is turned off (Fig.7 d). By comparing Fig.7 c to Fig.7 d, it can be seen that electron-induced diffusion plays a marginal role in these experimental conditions. It slightly promotes vacancy mobility, which results in a small number of clusters containing two vacancies ($n = -2$) and some O atoms. Most vacancy defects (more than 99, 99 %) contain only one vacancy ($n = -1$) and up to six O atoms ($p = 1 - 6$), due to the high mobility of O atoms. As expected, the increasing O concentrations lead to more decorated vacancy clusters, i.e. the number of clusters with large p values increases. In addition, the number of SIA clusters ($n \geq 2$) increases. They all contain at least one oxygen atom. Given the larger diffusion coefficient of SIAs with respect to oxygen atoms, the formation of such SIA clusters can be seen as a heterogeneous nucleation on O impurities. As the loop density increases with O concentration, the loop size decreases. The maximum number of SIAs in a cluster declines from around 95 to 30 as O concentration increases from 20 to 200 appm (Fig. 6 a-c). These smaller dislocation loops are more difficult to detect with TEM. The number of SIAs corresponding to a loop size of 1 nm, which can be considered as a detection limit in TEM, is shown by a vertical gray line on the cluster distributions. The density of SIA clusters larger than 1 nm decreases from 6×10^{22} m^{-3} to 3×10^{20} m^{-3} as oxygen concentration increases from 20 to 200 appm, and more than 99.95 % of them are smaller than 2 nm. Apart from the case $x_O = 20$ appm, loops of size larger than 1 nm are too scarce to be detectable in TEM.

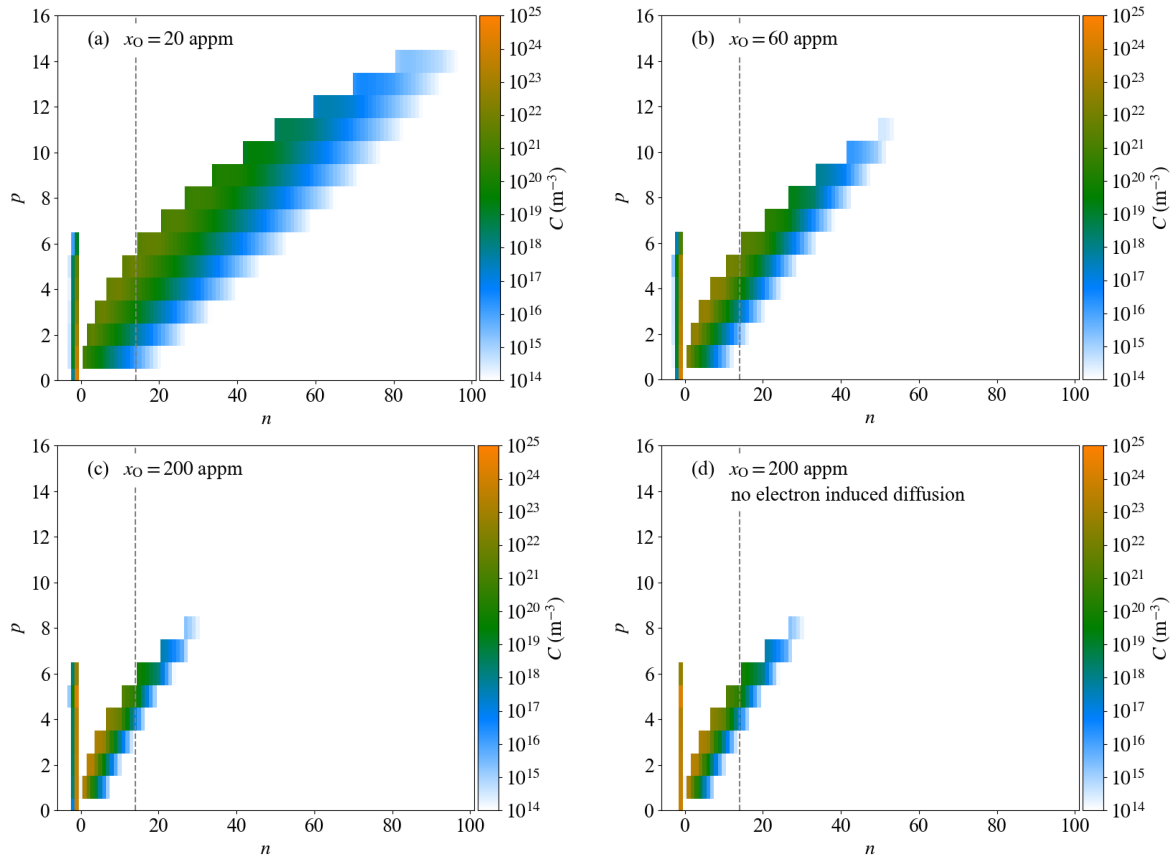

Fig.7: cluster size distributions at high fluence obtained by cluster dynamics. (a,b,c): Cluster distributions with a concentration of O in the matrix equal to 20, 60, and 200 appm respectively. (d): same as (c) but without taking into account electron-induced vacancy mobility. In these graphs, positive values of n refer to the number of SIAs in a cluster, whereas negative values are used for the number of vacancies (-n) in vacancy clusters. The number of O atoms in a cluster is noted in p. The vertical grey line corresponds to a loop of size 1 nm.

We also show the concentration of small vacancy-O complexes for low and high fluence conditions, as a function of the O concentration in the matrix (Fig.8). As expected, populations of complexes containing more O atoms increase with the concentration of O in the matrix. However, these populations decrease with the fluence. Indeed, owing to the low mobility of vacancies, these complexes tend to absorb more SIAs than vacancies. Assuming that the vacancy-O complexes are immobile at RT like the pure single vacancies, SIA that are highly mobile at RT can be absorbed by non-mobile oxygen-vacancies complexes. As a consequence, O atoms are released in the matrix and can freely migrate to dislocation loops or other vacancy clusters. On the contrary, the vacancy concentration steadily increases with the damage dose due to the continuous production of vacancies by irradiation and the low mobility of vacancies.

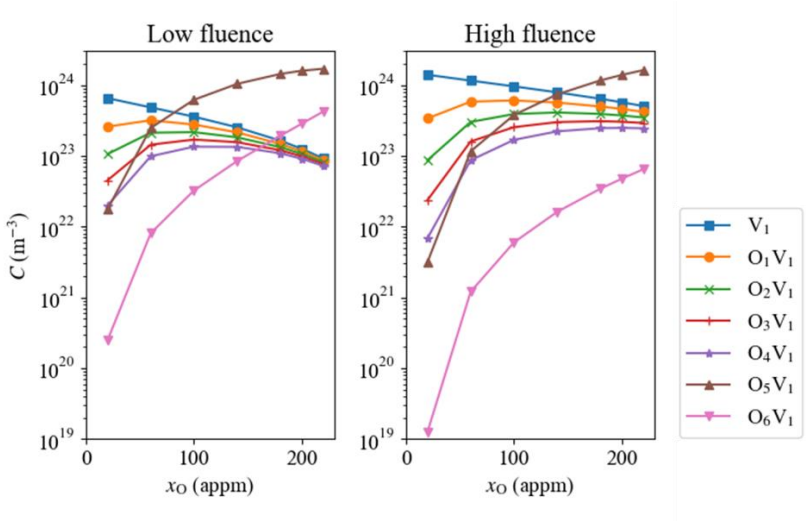

Fig.8: Concentration of vacancy-O clusters as a function of the atomic fraction of O in the matrix, for the low and high fluence cases. Clusters with more than one vacancy are not represented, as their concentration is negligible.

4. Discussion

Generally, low-energy electron irradiation generates mainly FPs. In our SPB-DBS experiments, in the near-surface region (0~700 nm), the presence of V_1 was detected by positrons at both fluences, and their concentration increased with the fluence. PALS results confirmed the annihilation of positrons as trapped at V_1 and, more interestingly, revealed new positron traps (***X defects***) with high annihilation probability. These traps have an average lifetime of about 122, and 135 ps for LF- and HF-damaged samples, respectively. Their nature is discussed below.

The ***X defects*** have a lifetime shorter by a factor of 1.44-1.64 than V_1 (195-200 ps), and it therefore could be related to defects with smaller open volumes than V_1. Two types of defects can be envisaged: (i) dislocation loops or (ii) impurity-vacancy complexes.

From TEM observations, no defects were detected in the **GF** disk irradiated at HF, indicating that the dislocation loop size and concentration were rather low i.e. lower than 1 nm and ~1×10^{19} m^{-3}, respectively. CD calculations predict a negligible concentration of interstitial clusters (around 1×10^{13} m^{-3}) all smaller than 1 nm in pure tungsten irradiated under experimental conditions, which is well below the experimental detection limits. Arakawa et *al.*[89] and Tamino et *al.*[90] observed an average density of dislocation loops of about 4×10^{22}

m^{-3} at 105 K in high-purity polycrystalline tungsten (99.9999 wt.%, JX Nippon Mining & Metals Co) irradiated with 2 MeV electrons at low temperatures (≤ 290 K) [89,90]. The average size of the dislocation loops is mentioned to be approximately 3–4 nm [89]. In these experiments, the fluence (~4×10^{25} m^{-2}) and the flux (1×10^{24} [89] and 3.0×10^{22} $m^{-2}.s^{-1}$ [90] respectively) are remarkably higher than those used in current work, by a factor of 200, and 3 to 6 orders of magnitude respectively. In such high flux irradiation conditions, the estimated damage rate is 1.3×10^{-4} dpa. s^{-1} (for 3.0×10^{22} $m^{-2}.s^{-1}$) in [89,90], which is five orders of magnitude higher than in the present study (2.3×10^{-9} dpa. s^{-1}). These differences give rise to a much higher local density of SIA in Arakawa's experiments, leading to a high probability of cluster formation. SIA interaction is much less likely to be under our irradiation conditions, and cluster formation remains limited in pure tungsten. Furthermore, CD results predict that an increase in O concentration promotes small SIA clusters (<1 nm) production for less pure tungsten, whereas it limits the formation of larger SIA clusters. It is expected that a cluster including more than 7 SIAs will reach a stable configuration and become an interstitial ½<111> loop [91] with a diameter of approximately 0.7 nm. The concentration of these clusters is predicted by CD to be at most 1.55×10^{23} m^{-3} for the O concentration of 60 appm. Could these TEM-invisible SIA clusters be detected by PAS? Their concentration is close to the PAS detection limit for V_1 (~10^{23} m^{-3}), but such a low concentration of defects could be detected only if their positron trapping coefficient, μ_{intL} was higher than that of V_1. Despite the μ_{intL}, is unknown to date, nevertheless, the positron binding energy E_B^p at an edge dislocation line has been calculated about -0.28 eV in iron by E. Kuramoto et *al.* [92]. Like the edge dislocation line, the interstitial loops have reduced free volume concerning the lattice on the line or at the loop periphery respectively, so a low E_B^p should also be expected for interstitial loops. This

suggests that the probability of a positron being trapped in such interstitial loops should be less probable, at least at RT. Thus, the ***X defects*** are unlikely to be dislocation loops.

According to TCDFT results, one V_1 can be associated with 1 to 6 O atoms, forming O-vacancy complexes with a lifetime close to the ***X defects***. CD simulation with 20 to 220 appm oxygen, predicts that all these O-vacancy complexes coexist. Next, we use the trapping model to calculate theoretical lifetime spectra ***PALS(t)*** for the damage dose of 4.1×10^{-4} and 8.3×10^{-4} dpa. In these models, we assume that the positron can annihilate in several states: $O_{1\text{-}6}V_1$ complexes, pure V_1, and ***Lattice***. The trapping rate $\boldsymbol{k_i}$ for each defect (V_1, $O_{1\text{-}6}V_1$) can be estimated by multiplying their concentration by their specific trapping coefficient, $\boldsymbol{\mu_i}$. The concentration of defects is given by CD simulations. The specific trapping coefficient for pure V_1 is $\boldsymbol{\mu_{V1}} = (6 \pm 3) \times 10^{-15}$ $m^{-3}.s^{-1}$ [31], and $\mu_{O_pV_1}$ for the O_pV_1 (with p = 1-6) complexes were estimated by reducing $\boldsymbol{\mu_{V1}}$ by a ratio of the Voronoi volume of each O complex to that of pure V_1 (Tab. *3*). Once the trapping rates $\boldsymbol{k_i}$ of each trap (t_1 = pure V_1 and $t_{2\text{-}7}$ = $O_{1\text{-}6}V_1$ complexes) are determined, the intensity of the lifetime components I_i, and the theoretical lifetime spectra ***PALS(t)*** can be calculated, using a trapping model including several annihilation states: ***Lattice***, pure V_1 and $O_{1\text{-}6}V_1$ complexes (eq. *2*)

$$\begin{cases} I_i = \frac{k_i}{\lambda_L - \lambda_i + \sum k_i} \text{ , and } I_0 + \sum_i I_i = 1 \\ \boldsymbol{PALS(t)} = R(t) * \left[\sum_i \left(\frac{I_i}{\tau_i} e^{-\frac{t}{\tau_i}} \right) + \sum_j \left(\frac{I_{C_j}}{\tau_{C_j}} e^{-\frac{t}{\tau_{C_j}}} \right) + \frac{I_0}{\tau_0} e^{-\frac{t}{\tau_0}} \right] + BG \end{cases} \quad \textit{eq. 2}$$

where defects *i* could be pure V_1, or $O_{1\text{-}6}V_1$ complexes, λ_L, and λ_i are the annihilation rate at the lattice and in each trap *i* respectively i.e. the reciprocal of their lifetime τ_L=105 ps for the lattice, and τ_i (τ_1 =200 ps for pure V_1, and the values of complexes reported in Tab. 3), and I_0 is the intensity of the reduced lifetime τ_0. τ_{Cj} and I_{Cj} are respectively the lifetimes and intensities for the source corrections. As a result, theoretical lifetime spectra were calculated by applying a trapping model with the parameters obtained from *eq. 2* for various concentrations of O,

573 and taking into account the spectrometer resolution (FWHM= 212 ps) and an experimental the
574 background noise of about 60 counts. Fig.9 a (LF) and b (HF) show the theoretical spectra for
575 a matrix containing 0 to 220 O appm in comparison with their respective experimental spectrum.

576 Firstly, in the absence of O, positrons annihilate only in pure V_1 and in the ***Lattice***. The
577 corresponding theoretical lifetime spectrum differs greatly from the experimental one: in the
578 region between 360 and 1400 ps, the number of counts is higher in the theoretical spectra than
579 in the experimental ones for both fluences, i.e. LF (Fig.9a.7) and HF (Fig.9b.7) as highlighted
580 in the residual standard deviation plotted above the lifetime spectra. It confirms that a
581 component with a lifetime between that of V_1 and that of the ***Lattice*** is hidden in the
582 experimental spectra, as extracted in the deconvolution fits of experimental spectra. This
583 component corresponds to new positron **traps X**.

584 Theoretical spectra with O concentration ranging from 20 to 220 appm agree much better
585 with experimental spectra than those without O. The best agreement corresponds to an O
586 concentration in the matrix of 140 appm, for HF (Fig.9a.1-4), and 100 appm, LF (Fig.9b.2-6)
587 shows a relatively lower residual between experimental and theoretical spectra. This
588 concentration range is comparable to the SIMS results measured with an error bar of 28 %
589 (Fig.4 c). Residual values can be explained by either experimental error bars or approximations
590 made in simulations, including CD and TCDFT, and also in estimating the specific trapping
591 coefficients. Despite all these approximations, these comparisons indicate that the trapping of
592 positrons in oxygen-vacancy complexes agrees with the experimental results and confirms that
593 **traps X** are oxygen-vacancy complexes.

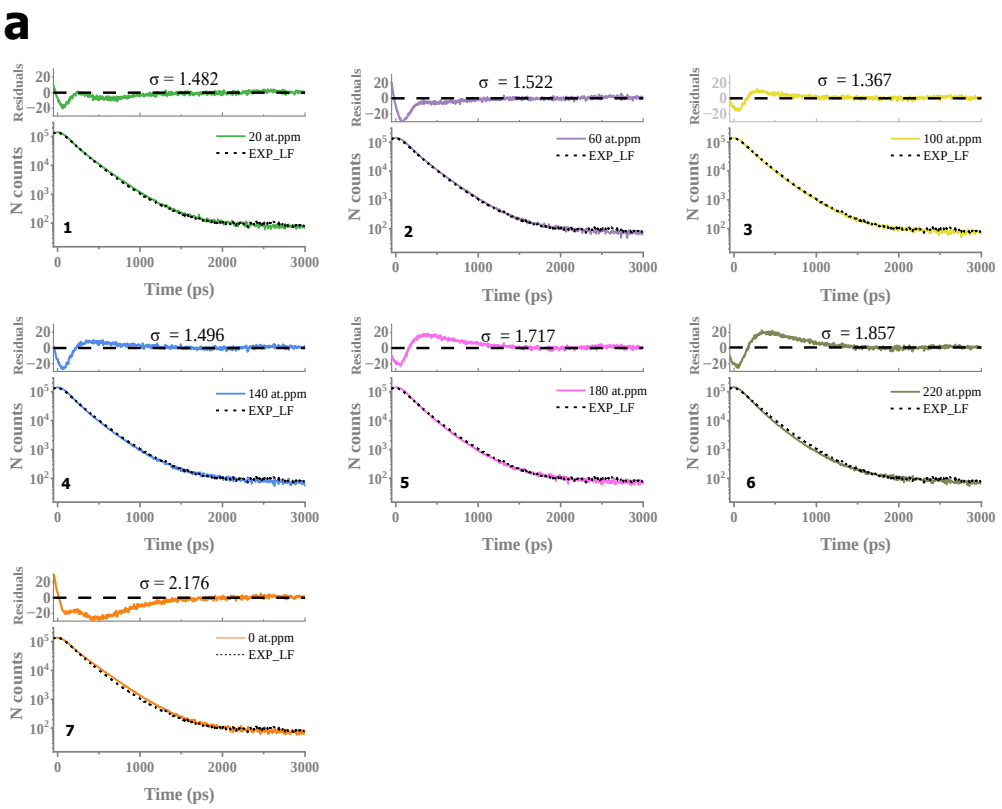

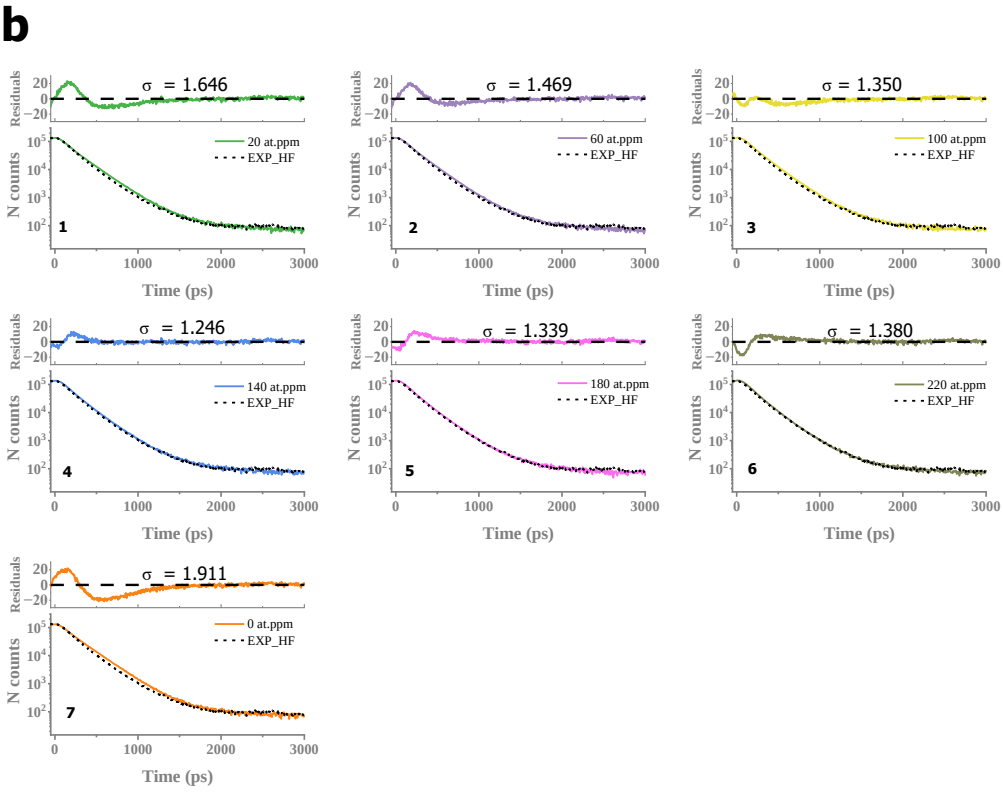

Fig.9: Comparison of theoretical and experimental lifetime spectra measured in **Nc** samples a: low fluence (LF). and b: high fluence (HF). The theoretical spectra were calculated by employing trapping models, with parameters calculated from *eq. 2*. The residual standard deviation (Residual) and its average absolute value (σ) highlight the difference between the two spectra on a time scale.

After comparing the lifetime spectra, we calculated the theoretical ***S-W*** values still based on the same two- or three-state trapping model (*eq.3*) depending on O concentration ranging from 0 to 220 appm using *eq. 3*.

$$\begin{cases} \boldsymbol{S} = S_L \cdot f_L + \sum S_i \cdot f_i \\ \boldsymbol{W} = W_L \cdot f_L + \sum W_i \cdot f_i \\ f_i = \frac{k_i}{\lambda_L + \sum k_i} \ , \ and \ f_L + \sum_{t_1}^{t_7} f_i = 1 \end{cases} \qquad eq.\ 3$$

where f_L and f_i are the fractions of annihilation in the delocalized state and the localized state of traps i respectively, determined using (*eq. 3*). The relative $\boldsymbol{S/S_L\text{-}W/W_L}$ points calculated for both fluences LF and HF are shown in Fig.10. a.

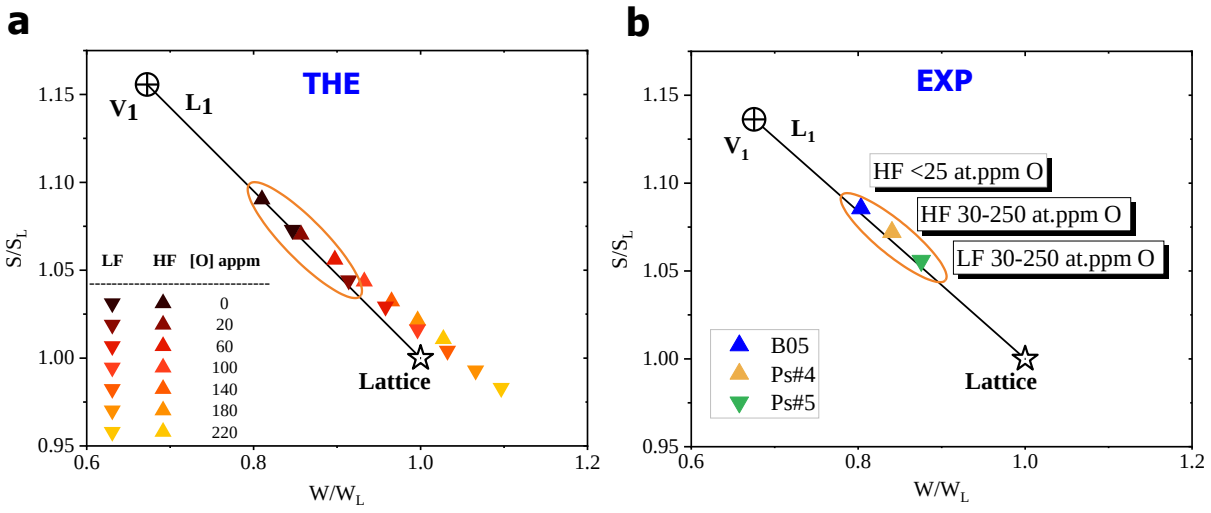

Fig.10 a: Theoretical relative ratio to lattice ***S-W*** using trapping model in the case of 0 to 220 appm O vs b: Experimental ***S-W*** points, an average of 5-25keV for B05, and at 25 keV for damaged Nc samples (HF: yellow triangle, LF: green triangle with 30-250 appm O, and HF: blue triangle with <25 appm O), the error of SIMS measurement is estimated to 28 %.

For zero O concentration, the ***S-W*** points calculated for both fluences LF and HF are located on line L_1. This is still the case when O concentration is low (20 appm). As shown in Fig.8, increasing O concentration induces a larger population of $O_{1\text{-}6}V_1$ complexes. Annihilations at these complexes shift ***S-W*** points to the right-bottom toward the ***Lattice*** point and progressively move away from L_1. We emphasize that only the relative $\boldsymbol{S/S_L\text{-}W/W_L}$ values can be used for comparison between theoretical and experimental data [37]. The $\boldsymbol{S/S_L\text{-}W/W_L}$ points measured

617 in **B05** (HF, <25 O appm) and in the **Nc** (LF & HF, 30-250 O appm) samples are shown in
618 Fig.10.

619 The experimental points are located on or near L_1. The purest sample **B05** (HF, <25 O
620 appm) shows the highest ***S*** and lowest ***W*** values, whereas ***S*** decreases and ***W*** increases for less
621 pure samples **Nc** (LF & HF, 30-250 O appm). The same trend can be observed for the theoretical
622 values (see Fig.10.a) showing a decrease of ***S*** and an increase of ***W*** with increasing oxygen
623 concentration. The agreement between calculated and experimental ***SW*** points appears to be
624 better for O concentrations of 20 and 60 appm. These concentration values are lower than those
625 for which better agreement was observed for lifetimes. This discrepancy might be due to
626 several factors: (i) the O distribution in **Nc** samples is heterogeneous and PALS probes a thick
627 region (~Ø 3 mm × 0.05 mm) whereas, in the SPB-DBS, positrons stopped close to the surface
628 (~Ø 3 mm, and 1st 700 nm); (ii) the errors propagate from approximations either in simulations
629 or experiments, making it difficult to achieve ideal agreement between experimental and
630 theoretical DB spectrum. Thus, only the trend on the variation of ***S*** and ***W*** can be discussed, as
631 shown by the comparisons made in [34,35].

632 We now focus on the experimental data for **B05**, containing the lowest O concentration. In
633 this sample, the relative position of the ***S-W*** point is close to the theoretical one calculated for
634 the zero O content. As the O concentration is below the SIMS detection limit (25 ± 8 appm),
635 we can assume that the $O_{1\text{-}6}V_1$ concentration is too low to have a significant annihilation
636 fraction, while pure V_1 should be the dominant trap. The pure V_1 concentration can simply be
637 extracted from the DB measurements by using a one-trap (pure V_1) trapping model [31,38],
638 using the following equation.

639 $$C_{V1} = \frac{\lambda_L.(X_L - X)}{\mu_{V1}(X - X_{V1})} \qquad \textit{eq. 4}$$

where X is ***S*** or ***W*** annihilation fractions and λ_L and μ_{V1} were already defined above.

The ***S*** and ***W*** values give a pure V_1 concentration of about (2.63 ± 1.32) × 10^{24} m^{-3}. This concentration is much lower than that expected from the damage dose calculated in the region probed by positrons (700 nm in tungsten, 8.33 × 10^{-4} dpa) which should be 5.28 × 10^{25} m^{-3} if each displacement effectively leads to a vacancy at the end of irradiation. This reduction of V_1 concentration reveals a high recombination rate R_c of FPs, which is estimated at around ~95 ± 2 %. This value is in excellent agreement with the theoretical results predicted by CD (96 %). In electron-irradiated pure iron, Takaki et *al*. [20] found in resistivity recovery experiments that 76 % of recombinations were related to uncorrelated FPs, and 19 % to correlated FPs, for a total of 95 %. Furthermore, Ortiz et *al.* [93] calculated that up to 90 % of defects have been annihilated at 400 K in Fe irradiated with electrons at a damage dose of 10^{-6} dpa. In tungsten, De Backer et *al.* [94] showed that R_c increases from 20 to 96 % for ^{3}He 800 keV irradiation at RT with various fluences, ranging from 10^{17} to 5 × 10^{20} m^{-2}, i.e. a range of damage dose from 1.9×10^{-4} to 0.17 dpa (SRIM with E_{disp} = 55.3 eV, K-P model). In addition, Neely et *al.* [19] found about 30 % of resistivity recovery in 99.99 % pure irradiated tungsten at 70 K (2.1 MeV e^-, 5 × 10^{21} $e^-.m^{-2}$), and the authors claimed that the recovery rate can be impacted by a non-negligible concentration of impurities.

In tungsten, at RT, the SIA has very low migration energy (< 0.2 eV [68,95,96]), whereas the vacancy is immobile. A high recombination rate can be expected. When oxygen or other impurities that interact strongly with SIA immobilize SIA, the probability of recombination decreases. In our CD results, the R_c ratio decreases from 96 to 87% when the O/FP ratio increases from 0 to 0.53. These results are consistent with the close relative position for theoretical and experimental ***S-W*** point observed for the lowest O content (0 appm HF, in Fig.10 a and **B05** in Fig.10 b). Despite all the approximations used in this work, agreement between simulations and experiments confirms that O affects the evolution of vacancy and interstitial

665 defects in tungsten irradiated at RT as illustrated in Fig.11. When a fraction of O atoms is
666 dissolved in the matrix, they can diffuse during irradiation. Electron irradiation induces
667 vacancies and SIAs. O atoms can be bound to V_1 and immobilize the SIA, leading to the
668 formation of oxygen-vacancy and O-SIA complexes in a proportion that increases with the
669 O/dpa ratio and the dpa rate. The presence of oxygen can increase the concentration of vacancy
670 defects by a factor of up to four and of the interstitial clusters by more than two orders of
671 magnitude depending on the ratio O/dpa, creating a large majority of O-decorated defects.

672 This effect has already been observed for carbon at high temperatures (>500°C [28]),
673 whereas the O effect is demonstrated here for the first time. It should be emphasized that this
674 effect is demonstrated here at RT. In industrial applications such as in fusion reactors, where
675 tungsten was chosen for the divertor and is envisaged for the first walls, this material will be
676 subjected to high temperature >500°C irradiation. Under these conditions, the O effect can be
677 expected to be pronounced. The diffusion coefficient will be higher for O than for C and ac-
678 cording to the simulations, O_pV_1 complexes have high binding energies of 3 to 12 eV (Tab. *3*)
679 close to those of C_PV_1 complexes, and even slightly higher [53]. Competition between C and O
680 can therefore be expected at higher temperatures when C atoms become mobile. Both elements
681 will impact the formation of the vacancy clusters and cavities. These O-decorated defects could
682 also have an impact on the retention of hydrogen in tungsten [23]. Predicting H retention in the
683 walls of fusion reactors is of major importance for safety, given the use of tritium, a radioactive
684 isotope of H, as fuel. Ab initio calculations show a strong interaction between O decorated
685 vacancies and H. Oxygen is one of the major impurities expected in tokamaks and is also diffi-
686 cult to avoid in tungsten. At least, for the large amount of material required in the reactor.
687 Accordingly, this work shows that oxygen has to be taken into account in the prediction of the
688 microstructure evolution of tungsten.

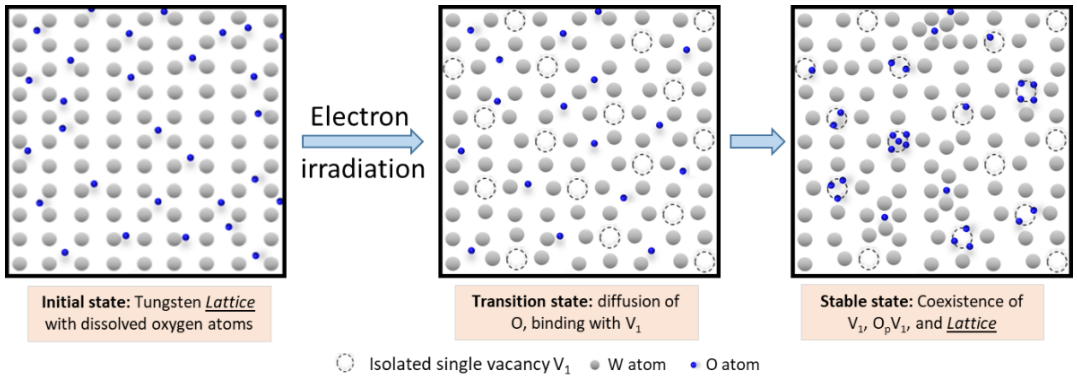

Fig.11: Schematic diagram of the evolution of the defects in tungsten samples irradiated with electrons in the presence of oxygen, as in the present work.

5. Conclusion

To summarize, after 2.5 MeV electron irradiation at RT, an unexpected positron annihilation state (X defect) was revealed by PALS measurement in tungsten. After combining other characterization techniques (TEM, SIMS) and simulations (TCDFT, CD), we have drawn the following conclusions regarding the microstructure evolution:

(i) According to CD simulations, the nucleation and growth of SIA clusters depend on the O atoms' presence in the matrix. This is in agreement with TEM results which show no evidence of dislocation loops.

(ii) Theoretical results (TCDFT, CD, and trapping model) with an O concentration of approx. 100-140 O appm shows a better match of experimental lifetime spectra (Fig.9), which is in good agreement with SIMS analysis. Consequently, the hypothesis of heterogeneous $O_{1-6}V_1$ complexes formation is verified.

(iii) PAS and CD results highlight the interaction between O atoms and V_1. In addition, in the O-free matrix, a very high recombination ratio, R_c of 95 ± 2 % was determined, in excellent agreement with the CD result (96 %).

(iv) As soon as the O concentration in the matrix is larger than 20 appm, the total population of $O_{1-6}V_1$ complexes exceeds that of pure V_1. The O effect on the evolution of SIAs and V_1 is therefore demonstrated at RT due to its high mobility and strong binding. This effect should

also be pronounced in high-temperature applications, and potentially be more important than that of the other LEs (H, C, and N).

Declaration of Competing Interest

The authors declare that they have no known competing financial interests or personal relationships that could have appeared to influence the work reported in this paper.

Credit authorship contribution statement

Zhiwei Hu: Sample preparation, PALS, SPB-DBS experiment, PAS and SIMS data processing and interpretation, writing – original draft & editing, ***Qigui Yang***: TCDFT calculation, data analysis, writing – original draft & editing ***Thomas Jourdan:*** CD calculation, data analysis, writing – original draft & editing ***Pierre Desgardin****:* Supervision, SPB-DBS experiments ***François Jomard:*** Supervision, SIMS experiments ***Cécile Genevois:*** Supervision, TEM experiments ***Jérôme Joseph:*** Sample preparation and technical support ***Pär Olsson***: Conceptualization, supervision, review & editing. ***Marie-France Barthe***: Conceptualization, supervision, data processing and interpretation, writing – review & editing.

Acknowledgments

The authors thank Olivier Cavani, Bruno Boizot, and Jérémy Lefebvre from the Laboratoire des Solides Irradiés (LSI) at École Polytechnique for electron irradiation EMIR&A network for the technical support during the irradiations. This work has been carried out within the framework of the EUROfusion Consortium, funded by the European Union via the Euratom Research and Training Programme (Grant Agreement No 101052200 — EUROfusion). Pär Olsson acknowledges funding from the Euratom research and training program 2019-2020 under grant agreement No 900018 (ENTENTE project). Views and opinions expressed are however those of the authors only and do not necessarily reflect those of the European Union or the European Commission. Neither the European Union nor the European Commission can be held responsible for them. Qigui Yang acknowledges the financial support by the China

Scholarship Council (No. 201807930008) and Svensk Kärnbränslehantering AB. The computational resources were provided by the Swedish National Infrastructure for Computing (SNIC) and by the CINECA HPC center in Italy. This project has benefited from the facilities of the Platform MACLE-CVL which was co-funded by the European Union and Centre-Val de Loire Region (FEDER). The authors thank Dr. Ilja.Makkonen at Helsinki University for sharing the positron code.

References

[1] M. Rieth, S.L. Dudarev, S.M. Gonzalez de Vicente, J. Aktaa, T. Ahlgren, S. Antusch, D.E.J. Armstrong, M. Balden, N. Baluc, M.-F. Barthe, W.W. Basuki, M. Battabyal, C.S. Becquart, D. Blagoeva, H. Boldyryeva, J. Brinkmann, M. Celino, L. Ciupinski, J.B. Correia, A. De Backer, C. Domain, E. Gaganidze, C. García-Rosales, J. Gibson, M.R. Gilbert, S. Giusepponi, B. Gludovatz, H. Greuner, K. Heinola, T. Höschen, A. Hoffmann, N. Holstein, F. Koch, W. Krauss, H. Li, S. Lindig, J. Linke, Ch. Linsmeier, P. López-Ruiz, H. Maier, J. Matejicek, T.P. Mishra, M. Muhammed, A. Muñoz, M. Muzyk, K. Nordlund, D. Nguyen-Manh, J. Opschoor, N. Ordás, T. Palacios, G. Pintsuk, R. Pippan, J. Reiser, J. Riesch, S.G. Roberts, L. Romaner, M. Rosiński, M. Sanchez, W. Schulmeyer, H. Traxler, A. Ureña, J.G. van der Laan, L. Veleva, S. Wahlberg, M. Walter, T. Weber, T. Weitkamp, S. Wurster, M.A. Yar, J.H. You, A. Zivelonghi, Recent progress in research on tungsten materials for nuclear fusion applications in Europe, Journal of Nuclear Materials 432 (2013) 482–500. https://doi.org/10.1016/j.jnucmat.2012.08.018.

[2] H. Bolt, V. Barabash, G. Federici, J. Linke, A. Loarte, J. Roth, K. Sato, Plasma facing and high heat flux materials – needs for ITER and beyond, Journal of Nuclear Materials 307–311 (2002) 43–52. https://doi.org/10.1016/S0022-3115(02)01175-3.

[3] M. Rieth, D. Armstrong, B. Dafferner, S. Heger, A. Hoffmann, M.D. Hoffmann, U. Jäntsch, C. Kübel, E. Materna-Morris, J. Reiser, M. Rohde, T. Scherer, V. Widak, H. Zimmermann, Tungsten as a Structural Divertor Material, AST 73 (2010) 11–21. https://doi.org/10.4028/www.scientific.net/AST.73.11.

[4] T. Hirai, S. Panayotis, V. Barabash, C. Amzallag, F. Escourbiac, A. Durocher, M. Merola, J. Linke, Th. Loewenhoff, G. Pintsuk, M. Wirtz, I. Uytdenhouwen, Use of tungsten material for the ITER divertor, Nuclear Materials and Energy 9 (2016) 616–622. https://doi.org/10.1016/j.nme.2016.07.003.

[5] A. Calvo, K. Schlueter, E. Tejado, G. Pintsuk, N. Ordás, I. Iturriza, R. Neu, J.Y. Pastor, C. García-Rosales, Self-passivating tungsten alloys of the system W-Cr-Y for high temperature applications, International Journal of Refractory Metals and Hard Materials 73 (2018) 29–37. https://doi.org/10.1016/j.ijrmhm.2018.01.018.

[6] C. Thomser, V. Bailescu, S. Brezinsek, J.W. Coenen, H. Greuner, T. Hirai, J. Linke, C.P. Lungu, H. Maier, G. Matthews, Ph. Mertens, R. Neu, V. Philipps, V. Riccardo, M. Rubel, C. Ruset, A. Schmidt, I. Uytdenhouwen, Plasma Facing Materials for the JET ITER-Like Wall, Fusion Science and Technology 62 (2012) 1–8. https://doi.org/10.13182/FST12-A14103.

[7] G.S. Was, Fundamentals of radiation materials science: metals and alloys, Springer, Berlin ; New York, 2007.

[8] X. Hu, T. Koyanagi, M. Fukuda, N.A.P.K. Kumar, L.L. Snead, B.D. Wirth, Y. Katoh, Irradiation hardening of pure tungsten exposed to neutron irradiation, Journal of Nuclear Materials 480 (2016) 235–243. https://doi.org/10.1016/j.jnucmat.2016.08.024.

[9] A. Hasegawa, Property change mechanism in tungsten under neutron irradiation in various reactors, Journal of Nuclear Materials (2011) 4.
[10] A. Hasegawa, M. Fukuda, S. Nogami, K. Yabuuchi, Neutron irradiation effects on tungsten materials, Fusion Engineering and Design 89 (2014) 1568–1572. https://doi.org/10.1016/j.fusengdes.2014.04.035.
[11] T. Miyazawa, L.M. Garrison, J.W. Geringer, M. Fukuda, Y. Katoh, T. Hinoki, A. Hasegawa, Neutron irradiation effects on the mechanical properties of powder metallurgical processed tungsten alloys, Journal of Nuclear Materials 529 (2020) 151910. https://doi.org/10.1016/j.jnucmat.2019.151910.
[12] J. Matolich, H. Nahm, J. Moteff, Swelling in neutron irradiated tungsten and tungsten-25 percent rhenium, Scripta Metallurgica 8 (1974) 837–841. https://doi.org/10.1016/0036-9748(74)90304-4.
[13] C. Chang, D. Terentyev, A. Zinovev, W.V. Renterghem, C. Yin, P. Verleysen, T. Pardoen, M. Vilémová, J. Matějíček, Irradiation-induced hardening in fusion relevant tungsten grades with different initial microstructures, Phys. Scr. 96 (2021) 124021. https://doi.org/10.1088/1402-4896/ac2181.
[14] J. Linke, J. Du, T. Loewenhoff, G. Pintsuk, B. Spilker, I. Steudel, M. Wirtz, Challenges for plasma-facing components in nuclear fusion, Matter and Radiation at Extremes 4 (2019) 056201. https://doi.org/10.1063/1.5090100.
[15] K. Farrell, A.C. Schaffhauser, J.O. Stiegler, Recrystallization, grain growth and the ductile-brittle transition in tungsten sheet, Journal of the Less Common Metals 13 (1967) 141–155. https://doi.org/10.1016/0022-5088(67)90177-4.
[16] G.S. Was, T. Allen, Intercomparison of microchemical evolution under various types of particle irradiation, Journal of Nuclear Materials 205 (1993) 332–338. https://doi.org/10.1016/0022-3115(93)90097-I.
[17] F. Maury, M. Biget, P. Vajda, A. Lucasson, P. Lucasson, Anisotropy of defect creation in electron-irradiated iron crystals, Phys. Rev. B 14 (1976) 5303–5313. https://doi.org/10.1103/PhysRevB.14.5303.
[18] F. Maury, M. Biget, P. Vajda, A. Lucasson, P. Lucasson, Frenkel pair creation and stage I recovery in W crystals irradiated near threshold, Radiation Effects 38 (1978) 53–65. https://doi.org/10.1080/00337577808233209.
[19] H.H. Neely, D.W. Keefer, A. Sosin, Electron Irradiation and Recovery of Tungsten, Phys. Stat. Sol. (b) 28 (1968) 675–682. https://doi.org/10.1002/pssb.19680280225.
[20] S. Takaki, J. Fuss, H. Kuglers, U. Dedek, H. Schultz, The resistivity recovery of high purity and carbon doped iron following low temperature electron irradiation, Radiation Effects 79 (1983) 87–122. https://doi.org/10.1080/00337578308207398.
[21] C.-C. Fu, J.D. Torre, F. Willaime, J.-L. Bocquet, A. Barbu, Multiscale modelling of defect kinetics in irradiated iron, Nat Mater 4 (2004) 68–74. https://doi.org/10.1038/nmat1286.
[22] W. Schilling, K. Sonnenberg, Recovery of irradiated and quenched metals, J. Phys. F: Met. Phys. 3 (1973) 322. https://doi.org/10.1088/0305-4608/3/2/005.
[23] G.-H. Lu, H.-B. Zhou, C.S. Becquart, A review of modelling and simulation of hydrogen behaviour in tungsten at different scales, Nucl. Fusion 54 (2014) 086001. https://doi.org/10.1088/0029-5515/54/8/086001.
[24] X.-S. Kong, Y.-W. You, Q.F. Fang, C.S. Liu, J.-L. Chen, G.-N. Luo, B.C. Pan, Z. Wang, The role of impurity oxygen in hydrogen bubble nucleation in tungsten, Journal of Nuclear Materials 433 (2013) 357–363. https://doi.org/10.1016/j.jnucmat.2012.10.024.
[25] T. Shimada, H. Kikuchi, Y. Ueda, A. Sagara, M. Nishikawa, Blister formation in tungsten by hydrogen and carbon mixed ion beam irradiation, Journal of Nuclear Materials 313–316 (2003) 204–208. https://doi.org/10.1016/S0022-3115(02)01447-2.
[26] M.Y. Ye, H. Kanehara, S. Fukuta, N. Ohno, S. Takamura, Blister formation on tungsten surface under low energy and high flux hydrogen plasma irradiation in NAGDIS-I, Journal of Nuclear Materials 313–316 (2003) 72–76. https://doi.org/10.1016/S0022-3115(02)01349-1.

[27] Z. Hu, P. Desgardin, C. Genevois, J. Joseph, B. Décamps, R. Schäublin, M.-F. Barthe, Effect of purity on the vacancy defects induced in self–irradiated tungsten: A combination of PAS and TEM, Journal of Nuclear Materials 556 (2021) 153175. https://doi.org/10.1016/j.jnucmat.2021.153175.
[28] N. Castin, A. Dubinko, G. Bonny, A. Bakaev, J. Likonen, A. De Backer, A.E. Sand, K. Heinola, D. Terentyev, The influence of carbon impurities on the formation of loops in tungsten irradiated with self-ions, Journal of Nuclear Materials 527 (2019) 151808. https://doi.org/10.1016/j.jnucmat.2019.151808.
[29] A. Bakaev, G. Bonny, N. Castin, D. Terentyev, V.A. Bakaev, Impact of interstitial impurities on the trapping of dislocation loops in tungsten, Sci Rep 11 (2021) 12333. https://doi.org/10.1038/s41598-021-91390-1.
[30] J. Zhang, W.-Z. Han, Oxygen solutes induced anomalous hardening, toughening and embrittlement in body-centered cubic vanadium, Acta Materialia 196 (2020) 122–132. https://doi.org/10.1016/j.actamat.2020.06.023.
[31] Hautojärvi, Corbel C., Positron Spectroscopy of Defects in Metals and Semiconductors, ENFI 125 (1995) 491–532. https://doi.org/10.3254/978-1-61499-211-0-491.
[32] F. Tuomisto, I. Makkonen, Defect identification in semiconductors with positron annihilation: Experiment and theory, Rev. Mod. Phys. 85 (2013) 1583–1631. https://doi.org/10.1103/RevModPhys.85.1583.
[33] D.J. Keeble, J. Wiktor, S.K. Pathak, L.J. Phillips, M. Dickmann, K. Durose, H.J. Snaith, W. Egger, Identification of lead vacancy defects in lead halide perovskites, Nat Commun 12 (2021) 5566. https://doi.org/10.1038/s41467-021-25937-1.
[34] Q. Yang, P. Olsson, Identification and evolution of ultrafine precipitates in Fe-Cu alloys by first-principles modelling of positron annihilation, Acta Materialia (2022) 118429. https://doi.org/10.1016/j.actamat.2022.118429.
[35] M. Elsayed, T.E.M. Staab, J. Čížek, R. Krause-Rehberg, Monovacancy-hydrogen interaction in pure aluminum: Experimental and ab-initio theoretical positron annihilation study, Acta Materialia 248 (2023) 118770. https://doi.org/10.1016/j.actamat.2023.118770.
[36] T. Jourdan, C.C. Fu, L. Joly, J.L. Bocquet, M.J. Caturla, F. Willaime, Direct simulation of resistivity recovery experiments in carbon-doped α-iron, Phys. Scr. T145 (2011) 014049. https://doi.org/10.1088/0031-8949/2011/T145/014049.
[37] Q. Yang, Z. Hu, I. Makkonen, P. Desgardin, W. Egger, M.-F. Barthe, P. Olsson, A combined experimental and theoretical study of small and large vacancy clusters in tungsten, Journal of Nuclear Materials (2022) 154019. https://doi.org/10.1016/j.jnucmat.2022.154019.
[38] R. Krause-Rehberg, H.S. Leipner, Positron Annihilation in Semiconductors: Defect Studies, Springer-Verlag, Berlin Heidelberg, 1999. http://www.springer.com/gp/book/9783540643715 (accessed October 19, 2021).
[39] B. Boizot, M. Soyer, L'accélérateur d'électrons SIRIUS du Laboratoire des Solides Irradiés: Un outil unique pour l'étude des effets d'irradiation dans les matériaux, Reflets phys. (2013) 28–29. https://doi.org/10.1051/refdp/201332028.
[40] W.A. McKinley, H. Feshbach, The Coulomb Scattering of Relativistic Electrons by Nuclei, Phys. Rev. 74 (1948) 1759–1763. https://doi.org/10.1103/PhysRev.74.1759.
[41] P.D. Lesueur, Cascades de déplacement dam les solides polyatomiques, Philosophical Magazine A 44 (1981) 905–929. https://doi.org/10.1080/01418618108239557.
[42] A. Dunlop, D. Lesueur, J. Dural, Damage production in iron during high-energy ion irradiation: Experimental and theoretical determinations, Nuclear Instruments and Methods in Physics Research Section B: Beam Interactions with Materials and Atoms 42 (1989) 182–192. https://doi.org/10.1016/0168-583X(89)90705-2.
[43] D.R. Mason, X. Yi, M.A. Kirk, S.L. Dudarev, Elastic trapping of dislocation loops in cascades in ion-irradiated tungsten foils, J. Phys.: Condens. Matter 26 (2014) 375701. https://doi.org/10.1088/0953-8984/26/37/375701.

[44] A. Hollingsworth, M.-F. Barthe, M.Y. Lavrentiev, P.M. Derlet, S.L. Dudarev, D.R. Mason, Z. Hu, P. Desgardin, J. Hess, S. Davies, B. Thomas, H. Salter, E.F.J. Shelton, K. Heinola, K. Mizohata, A. De Backer, A. Baron-Wiechec, I. Jepu, Y. Zayachuk, A. Widdowson, E. Meslin, A. Morellec, Comparative study of deuterium retention and vacancy content of self-ion irradiated tungsten, Journal of Nuclear Materials 558 (2022) 153373. https://doi.org/10.1016/j.jnucmat.2021.153373.
[45] P. Desgardin, L. Liszkay, M.F. Barthe, L. Henry, J. Briaud, M. Saillard, L. Lepolotec, C. Corbel, G. Blondiaux, A. Colder, P. Marie, M. Levalois, Slow Positron Beam Facility in Orléans, MSF 363–365 (2001) 523–525. https://doi.org/10.4028/www.scientific.net/MSF.363-365.523.
[46] E. Soininen, J. Mäkinen, D. Beyer, P. Hautojärvi, High-temperature positron diffusion in Si, GaAs, and Ge, Phys. Rev. B 46 (1992) 13104–13118. https://doi.org/10.1103/PhysRevB.46.13104.
[47] A. van Veen, H. Schut, J. de Vries, R.A. Hakvoort, M.R. Ijpma, Analysis of positron profiling data by means of '"VEPFIT,"' in: AIP Conference Proceedings, AIP, Ontario (Canada), 1991: pp. 171–198. https://doi.org/10.1063/1.40182.
[48] A. van Veen, H. Schut, M. Clement, J.M.M. de Nijs, A. Kruseman, M.R. IJpma, VEPFIT applied to depth profiling problems, Applied Surface Science 85 (1995) 216–224. https://doi.org/10.1016/0169-4332(94)00334-3.
[49] T.E.M. Staab, B. Somieski, R. Krause-Rehberg, The data treatment influence on the spectra decomposition in positron lifetime spectroscopy Part 2: The effect of source corrections, Nuclear Instruments and Methods in Physics Research Section A: Accelerators, Spectrometers, Detectors and Associated Equipment 381 (1996) 141–151. https://doi.org/10.1016/0168-9002(96)00585-2.
[50] S. McGuire, D.J. Keeble, Positron lifetimes of polycrystalline metals: A positron source correction study, Journal of Applied Physics 100 (2006) 103504. https://doi.org/10.1063/1.2384794.
[51] M. Bertolaccini, L. Zappa, Source-supporting foil effect on the shape of positron time annihilation spectra, Nuov Cim B 52 (1967) 487–494. https://doi.org/10.1007/BF02711092.
[52] A. Alkhamees, H.-B. Zhou, Y.-L. Liu, S. Jin, Y. Zhang, G.-H. Lu, Vacancy trapping behaviors of oxygen in tungsten: A first-principles study, Journal of Nuclear Materials 437 (2013) 6–10. https://doi.org/10.1016/j.jnucmat.2013.01.317.
[53] Y.-W. You, X.-S. Kong, X.-B. Wu, C.S. Liu, Q.F. Fang, J.L. Chen, G.-N. Luo, Interaction of carbon, nitrogen and oxygen with vacancies and solutes in tungsten, RSC Adv. 5 (2015) 23261–23270. https://doi.org/10.1039/C4RA13854F.
[54] A. Alkhamees, Y.-L. Liu, H.-B. Zhou, S. Jin, Y. Zhang, G.-H. Lu, First-principles investigation on dissolution and diffusion of oxygen in tungsten, Journal of Nuclear Materials 393 (2009) 508–512. https://doi.org/10.1016/j.jnucmat.2009.07.012.
[55] S. Gorondy-Novak, F. Jomard, F. Prima, H. Lefaix-Jeuland, SIMS as a new methodology to depth profile helium in as-implanted and annealed pure bcc metals?, Nuclear Instruments and Methods in Physics Research Section B: Beam Interactions with Materials and Atoms 398 (2017) 56–64. https://doi.org/10.1016/j.nimb.2017.02.036.
[56] S. Hasanzadeh, R. Schäublin, B. Décamps, V. Rousson, E. Autissier, M.F. Barthe, C. Hébert, Three-dimensional scanning transmission electron microscopy of dislocation loops in tungsten, Micron 113 (2018) 24–33. https://doi.org/10.1016/j.micron.2018.05.010.
[57] G. Kresse, J. Furthmüller, Efficient iterative schemes for ab initio total-energy calculations using a plane-wave basis set, Physical Review B 54 (1996) 11169–11186. https://doi.org/10.1103/PhysRevB.54.11169.
[58] P.E. Blöchl, Projector augmented-wave method, Physical Review B 50 (1994) 17953–17979. https://doi.org/10.1103/PhysRevB.50.17953.
[59] J.P. Perdew, K. Burke, M. Ernzerhof, Generalized Gradient Approximation Made Simple, Physical Review Letters 77 (1996) 3865–3868. https://doi.org/10.1103/PhysRevLett.77.3865.

[60] I. Makkonen, M. Hakala, M.J. Puska, Modeling the momentum distributions of annihilating electron-positron pairs in solids, Physical Review B 73 (2006) 035103. https://doi.org/10.1103/PhysRevB.73.035103.
[61] P. Folegati, I. Makkonen, R. Ferragut, M.J. Puska, Analysis of electron-positron momentum spectra of metallic alloys as supported by first-principles calculations, Physical Review B 75 (2007) 054201. https://doi.org/10.1103/PhysRevB.75.054201.
[62] E. Boroński, R.M. Nieminen, Electron-positron density-functional theory, Physical Review B 34 (1986) 3820–3831. https://doi.org/10.1103/PhysRevB.34.3820.
[63] M.J. Puska, A.P. Seitsonen, R.M. Nieminen, Electron-positron Car-Parrinello methods: Self-consistent treatment of charge densities and ionic relaxations, Physical Review B 52 (1995) 10947–10961. https://doi.org/10.1103/PhysRevB.52.10947.
[64] M. Alatalo, B. Barbiellini, M. Hakala, H. Kauppinen, T. Korhonen, M.J. Puska, K. Saarinen, P. Hautojärvi, R.M. Nieminen, Theoretical and experimental study of positron annihilation with core electrons in solids, Physical Review B 54 (1996) 2397–2409. https://doi.org/10.1103/PhysRevB.54.2397.
[65] T. Jourdan, G. Bencteux, G. Adjanor, Efficient simulation of kinetics of radiation induced defects: A cluster dynamics approach, Journal of Nuclear Materials 444 (2014) 298–313. https://doi.org/10.1016/j.jnucmat.2013.10.009.
[66] M. Kiritani, Electron Radiation Induced Diffusion of Point Defects in Metals, J. Phys. Soc. Jpn. 40 (1976) 1035–1042. https://doi.org/10.1143/JPSJ.40.1035.
[67] L. Reali, M.R. Gilbert, M. Boleininger, S.L. Dudarev, Intense γ -Photon and High-Energy Electron Production by Neutron Irradiation: Effects of Nuclear Excitations on Reactor Materials, PRX Energy 2 (2023) 023008. https://doi.org/10.1103/PRXEnergy.2.023008.
[68] C.S. Becquart, C. Domain, U. Sarkar, A. DeBacker, M. Hou, Microstructural evolution of irradiated tungsten: Ab initio parameterisation of an OKMC model, Journal of Nuclear Materials 403 (2010) 75–88. https://doi.org/10.1016/j.jnucmat.2010.06.003.
[69] H. Trinkaus, H.L. Heinisch, A.V. Barashev, S.I. Golubov, B.N. Singh, 1D to 3D diffusion-reaction kinetics of defects in crystals, Phys. Rev. B 66 (2002) 060105. https://doi.org/10.1103/PhysRevB.66.060105.
[70] G. Adjanor, Complete characterization of sink-strengths for 1D to 3D mobilities of defect clusters: Bridging between limiting cases with effective sink-strengths calculations., Journal of Nuclear Materials 572 (2022) 154010. https://doi.org/10.1016/j.jnucmat.2022.154010.
[71] H. Schultz, H. Ullmaier, Atomic Defects in Metals · W: Datasheet from Landolt-Börnstein - Group III Condensed Matter · Volume 25: “Atomic Defects in Metals” in SpringerMaterials (https://doi.org/10.1007/10011948_54), (n.d.). https://doi.org/10.1007/10011948_54.
[72] P.M. Derlet, D. Nguyen-Manh, S.L. Dudarev, Multiscale modeling of crowdion and vacancy defects in body-centered-cubic transition metals, Phys. Rev. B 76 (2007) 054107. https://doi.org/10.1103/PhysRevB.76.054107.
[73] R. Alexander, M.-C. Marinica, L. Proville, F. Willaime, K. Arakawa, M.R. Gilbert, S.L. Dudarev, Ab initio scaling laws for the formation energy of nanosized interstitial defect clusters in iron, tungsten, and vanadium, Phys. Rev. B 94 (2016) 024103. https://doi.org/10.1103/PhysRevB.94.024103.
[74] P.-E. Lhuillier, Etude du comportement de l’hélium et des défauts lacunaires dans le tungstène, phdthesis, Université d’Orléans, 2010. https://tel.archives-ouvertes.fr/tel-00587482 (accessed January 7, 2021).
[75] P.E. Lhuillier, M.F. Barthe, P. Desgardin, W. Egger, P. Sperr, Positron annihilation studies on the nature and thermal behaviour of irradiation induced defects in tungsten, Phys. Status Solidi (c) 6 (2009) 2329–2332. https://doi.org/10.1002/pssc.200982114.
[76] O.V. Ogorodnikova, M. Majerle, V.V. Gann, J. Čížek, P. Hruška, S. Simakov, M. Štefánik, V. Zach, Verification of the theory of primary radiation damage by comparison with experimental data, Journal of Nuclear Materials 525 (2019) 22–31. https://doi.org/10.1016/j.jnucmat.2019.07.019.

[77] P.M.G. Nambissan, P. Sen, Positron annihilation study of the annealing behaviour of alpha induced defects in tungsten, Radiation Effects and Defects in Solids 124 (1992) 215–221. https://doi.org/10.1080/10420159208220193.
[78] R. Ziegler, H.E. Schaefer, Vacancy Formation in Molybdenum and Tungsten Investigated by Positron Lifetime Measurements, MSF 15–18 (1987) 145–148. https://doi.org/10.4028/www.scientific.net/MSF.15-18.145.
[79] H.-E. Schaefer, Investigation of Thermal Equilibrium Vacancies in Metals by Positron Annihilation, Phys. Stat. Sol. (a) 102 (1987) 47–65. https://doi.org/10.1002/pssa.2211020104.
[80] C.S. Becquart, C. Domain, Ab initio calculations about intrinsic point defects and He in W, Nuclear Instruments and Methods in Physics Research Section B: Beam Interactions with Materials and Atoms 255 (2007) 23–26. https://doi.org/10.1016/j.nimb.2006.11.006.
[81] Q. Yang, Z. Hu, I. Makkonen, P. Desgardin, W. Egger, M.-F. Barthe, P. Olsson, A combined experimental and theoretical study of small and large vacancy clusters in tungsten, Journal of Nuclear Materials 571 (2022) 154019. https://doi.org/10.1016/j.jnucmat.2022.154019.
[82] K. Sato, A. Hirosako, K. Ishibashi, Y. Miura, Q. Xu, M. Onoue, Y. Fukutoku, T. Onitsuka, M. Hatakeyama, S. Sunada, T. Yoshiie, Quantitative evaluation of hydrogen atoms trapped at single vacancies in tungsten using positron annihilation lifetime measurements: Experiments and theoretical calculations, Journal of Nuclear Materials 496 (2017) 9–17. https://doi.org/10.1016/j.jnucmat.2017.09.002.
[83] P. Staikov, N. Djourelov, Simulations of 〈100〉 edge and 1/2〈111〉 screw dislocations in α-iron and tungsten and positron lifetime calculations, Physica B: Condensed Matter 413 (2013) 59–63. https://doi.org/10.1016/j.physb.2012.12.026.
[84] A. Yabuuchi, M. Tanaka, A. Kinomura, Short positron lifetime at vacancies observed in electron-irradiated tungsten: Experiments and first-principles calculations, Journal of Nuclear Materials 542 (2020) 152473. https://doi.org/10.1016/j.jnucmat.2020.152473.
[85] A. Dunand, M. Minissale, J.-B. Faure, L. Gallais, T. Angot, R. Bisson, Surface oxygen versus native oxide on tungsten: contrasting effects on deuterium retention and release, Nucl. Fusion 62 (2022) 054002. https://doi.org/10.1088/1741-4326/ac583a.
[86] N. Igata, S. Sato, FIM observation of point defect clusters in ion-implanted tungsten surfaces, Nanotechnology 4 (1993) 213–217. https://doi.org/10.1088/0957-4484/4/4/006.
[87] Z. Zhou, S.L. Dudarev, M.L. Jenkins, A.P. Sutton, M.A. Kirk, Diffraction imaging and diffuse scattering by small dislocation loops, Journal of Nuclear Materials 367–370 (2007) 305–310. https://doi.org/10.1016/j.jnucmat.2007.03.135.
[88] A. Yabuuchi, Inverse change in positron lifetimes of vacancies in tungsten by binding of interstitial impurity atoms to a vacancy: A first-principles study, Nuclear Materials and Energy 34 (2023) 101364. https://doi.org/10.1016/j.nme.2023.101364.
[89] K. Arakawa, M.-C. Marinica, S. Fitzgerald, L. Proville, D. Nguyen-Manh, S.L. Dudarev, P.-W. Ma, T.D. Swinburne, A.M. Goryaeva, T. Yamada, T. Amino, S. Arai, Y. Yamamoto, K. Higuchi, N. Tanaka, H. Yasuda, T. Yasuda, H. Mori, Quantum de-trapping and transport of heavy defects in tungsten, Condensed Matter Physics (n.d.). https://doi.org/10.1038/s41563-019-0584-0.
[90] T. Amino, K. Arakawa, H. Mori, Activation energy for long-range migration of self-interstitial atoms in tungsten obtained by direct measurement of radiation-induced point-defect clusters, Philosophical Magazine Letters 91 (2011) 86–96. https://doi.org/10.1080/09500839.2010.533133.
[91] C. Domain, C.S. Becquart, Solute – 〈111〉 interstitial loop interaction in α-Fe: A DFT study, Journal of Nuclear Materials 499 (2018) 582–594. https://doi.org/10.1016/j.jnucmat.2017.10.070.
[92] E. Kuramoto, T. Tsutsumi, K. Ueno, M. Ohmura, Y. Kamimura, Positron lifetime calculations on vacancy clusters and dislocations in Ni and Fe, Computational Materials Science 14 (1999) 28–35. https://doi.org/10.1016/S0927-0256(98)00068-8.

[93] C.J. Ortiz, M.J. Caturla, Cascade damage evolution: rate theory versus kinetic Monte Carlo simulations, J Computer-Aided Mater Des 14 (2007) 171–181. https://doi.org/10.1007/s10820-007-9082-9.
[94] A. De Backer, P.E. Lhuillier, C.S. Becquart, M.F. Barthe, Modelling of the implantation and the annealing stages of 800keV 3He implanted tungsten: Formation of nanovoids in the near surface region, Journal of Nuclear Materials 429 (2012) 78–91. https://doi.org/10.1016/j.jnucmat.2012.05.024.
[95] R.A. Johnson, Point-defect calculations for tungsten, Phys. Rev. B 27 (1983) 2014–2018. https://doi.org/10.1103/PhysRevB.27.2014.
[96] K. Heinola, T. Ahlgren, K. Nordlund, J. Keinonen, Hydrogen interaction with point defects in tungsten, Phys. Rev. B 82 (2010) 094102. https://doi.org/10.1103/PhysRevB.82.094102.